Microwave Photonic Characterization of High Temperature Superconducting Optoelectronic Devices

by

Haig A. Atikian

A thesis
presented to the University of Waterloo
in fulfillment of the
thesis requirement for the degree of
Master of Applied Science
in
Electrical and Computer Engineering

Waterloo, Ontario, Canada, 2009

AUTHOR'S DECLARATION

I hereby declare that I am the sole author of this thesis. This is a true copy of the thesis, including any required final revisions, as accepted by my examiners.
I understand that my thesis may be made electronically available to the public.

Haig A. Atikian

Abstract

The increasing demand for high performance communications systems and signal processing is constantly driving researchers to develop novel devices in both the microwave and optical domains. The possibility of using high temperature superconductors (HTS) as a platform for ultra-fast, ultra-high sensitive optoelectronic and microwave photonic devices has been explored.

This report introduces a cryogenic microwave photonic probe station, designed and built to characterize HTS microwave photonic devices. A methodology is presented to design coplanar waveguide transmission lines using HTS. The transmission line is then modified to include a meander line structure to serve the optoelectronic function. The device is characterized in several different operating domains, as an optically tunable microwave resonator, an optically tunable delay line, and finally as a photodetector.

A planar HTS weak leak structure is investigated with the measurements of the I-V characteristics. Moreover, this device is proposed as the next generation platform to fabricate ultra-fast and ultra-high sensitive photodetectors using HTS.

Acknowledgements

Firstly, I would like to express my deep and sincere gratitude to my supervisor, Professor A. Hamed Majedi. I am thankful for his support, guidance, and his confidence in me through all the phases of my research.

I would like to thank Prof. Chris J. Stevens from the University of Oxford for taking me into his lab and introducing me to the field of superconductivity. His supervision and guidance was instrumental in the development of my abilities in this field. I would also like to thank Professor Steven M. Anlage from the University of Maryland for accepting me into his lab and his providing his expertise assisting me to perform measurements on superconducting samples.

I would like to thank members from my group, Behnood G. Ghamsari and Hamid Reza Mohebbi, for their help in the theory and design of several devices measured in my work. I would also like to thank Jean-Luc Orgiazzi for his help in the lab, specifically with his assistance with the cryostat, and optical probe arm.

Finally, I would like to thank the readers Prof. Hany Aziz and Prof. Bo Cui for taking the time to review this report.

Dedication

To my family

Table of Contents

List of Figures

List of Tables

Chapter 1
Introduction

Superconductors differ from all other known conductors by a fundamental difference in the quantum nature of how electrons move through the material. This difference gives rise to unique properties creating a new area of research where engineers and scientists alike strive to find practical applications exploiting this phenomenon. This unique property causes certain materials to exhibit zero resistance at low temperatures, earning them the classification of a superconductor.

The zero resistance state allows for high current densities well suited for commercial applications such as electric power transmission. The possibility to make powerful magnets lends themselves for practical applications such as magnetic levitation for transportation and medical diagnostic equipment. The low loss and extremely low dispersion characteristics of superconductors make them an attractive option for high performance microwave components such as delay lines, phase shifters, detectors, mixers, low power amplifiers and oscillators. Superconductivity enables a range of innovative technology applications in many areas, where its full commercial potential is just beginning to be utilized.

1.1 Introduction to Superconductivity

Superconductivity was discovered in 1911 by a Dutch physicist, Heike Kamerlingh Onnes [1]. He cooled a sample of mercury metal and noticed at 4.2K the resistance abruptly vanished. Electric current could flow through the sample without any dissipation below a certain temperature called the critical temperature (T_c). He called this phenomenon superconductivity and in 1913 was awarded the Nobel Prize.

The next historical discovery was perfect diamagnetism, discovered by W. Meisser and R. Ochsenfeld [2]. They observed that a magnetic field is expelled from a superconductor that undergoes a normal to superconducting transition. This effect, now known as the Meissner effect, represents a different state than just perfect conductivity and is evident in all superconductors.

There was much effort placed in the research to explain why superconductivity occurs. In 1935, two brothers F. and H. London gave a description of two electrodynamic properties of superconductors used in conjunction with Maxwell's equation for superconducting structures [3], [4]. In 1957, the fundamental microscopic theory of superconductivity was developed called the BCS theory, named after its three developers J. Bardeen, L.N. Cooper, and J.R. Schrieffer [5]. This was the second Nobel Prize awarded in the field of superconductivity. The theory provided an accurate explanation of observed properties in elementary superconductors, belonging to a class of superconductors commonly known as low temperature superconductors (LTS).

In 1986, G. Bednorz and A. Mullerat at IBM in Zurich Switzerland, discovered superconductivity in a brittle ceramic compound at 35K [6]. Soon after, P. Chu discovered the first high-temperature superconductor (HTS) with a critical temperature of around 92K. As opposed to conventional superconductors, HTSs have higher transition temperatures (T_c), longer penetration depths (λ), and short coherence lengths (ξ). However the phase transition of HTSs is still not understood. Much effort has been placed in investigating this new class of material. The ease of cooling to liquid nitrogen temperature to achieve superconductivity has significantly influenced developments in fabrication, and created a market for practical applications. The history for high temperature superconductors is only just beginning.

1.2 Superconducting Microwave Photonics

Developments in microwave superconductivity and photonic technology are presenting an opportunity for superconducting optoelectronics and microwave photonics [7]. Superconducting optoelectronics entails any electronic function performed in conjunction with optical illumination via the photo-absorption phenomenon using superconductors. Superconducting microwave photonics evolves the manipulation of a microwave signal in a superconducting transmission line system by optical illumination. Superconductors lend themselves to both applications by virtue of their unique properties of low-loss electrical propagation and ultrafast photoresponse to allow an interaction between the electrical and optical domains. Superconductors exhibit a photoabsorption phenomenon, similar to semiconductors, creating the framework to build novel optoelectronic devices [8]. These devices include integrated optoelectronic photodetectors, mixers, modulators [9], [10] and optically tuned microwave devices such as tunable delay lines and tunable resonators [11], [12]. Since superconducting devices operate at cryogenic temperatures, it inherently provides a low noise environment well suited for high performance microwave and optical communication systems.

1.3 Objectives and Thesis Organization

The main motivation and goal of this thesis is two fold. Firstly, it is to design and build a cryogenic microwave photonic test system to facilitate the microwave and optical measurements of superconducting optoelectronic devices. This experimental setup will utilize micro-manipulated cryogenic probes such that measurements can be done directly on wafer. Device specific packaging and housings will not be needed, increasing the measurement accuracy and efficiency. The setup will also provide a means to introduce an optical fiber into the cryogenic measurement setup such that the superconducting devices can be excited with a laser. Second, is to design, fabricate and characterize several microwave superconducting optoelectronic devices.

The thesis is organized into six chapters. The first chapter provided a brief introduction into superconductivity, stated the research motivations and applications for microwave optoelectronics, and provided a quick overview of the objectives of this thesis. The second chapter will describe the microwave photonic probe station designed to perform the measurements. All the technical considerations required to successful create a working vacuum, cryogenic, microwave and optical setup will be discussed in this section. The third section will provide a methodology to design an HTS coplanar transmission line and compare experimental results to the theory. Section four will modify the transmission line to include a meander line to serve the optoelectronic function. This device will be characterized as an optically tunable microwave resonator and delay line. Chapter five will briefly introduce the meander line presented in chapter four as a picosecond photodetector. Chapter six describes the initial investigations on a weak link structure fabricated from HTS, and its potential application to make an ultra-fast and ultra-high sensitive photodetector from HTS.

Chapter 2

Cryogenic Microwave Photonic Probe Station

The ability to perform microwave measurements at cryogenic temperature is of critical importance in superconducting microwave photonics and optoelectronics. In any microwave characterization, it is advantageous to perform measurements directly on the device of interest with the absence of packaging and wire bonds. This ensures the measurement data purely represents the device behavior and not artifacts of the test fixture. The use of a cryogenic probe station not only eliminates the need for device packaging and wire bonds, but also provides a suitable platform for calibration at cryogenic temperatures. It also provides the flexibility of testing several devices quickly, efficiently, in one experiment run [13]-[15]. The following section will describe the design and functionality of the cryogenic microwave photonic probe station used to characterize HTS devices. A full description of the system is given, along with cool down curves for the sample stage and microwave probes. Also, the unique method of attaining an accurate calibration at cryogenic temperatures is discussed.

2.1 System Description

A block diagram of the microwave photonic probe station is shown in Fig. 2.1. The image is adopted from [16].

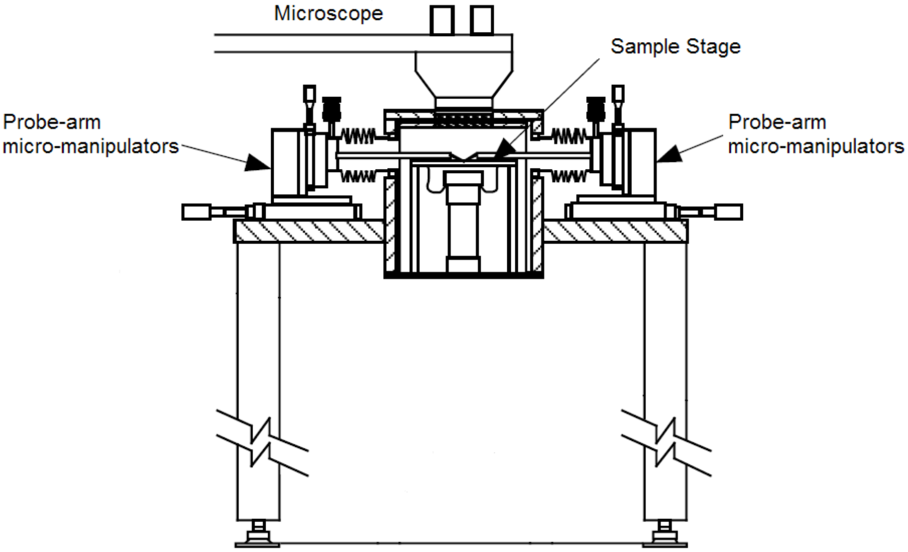

Figure 2.1 Block diagram of cryogenic microwave probe station [16]

The setup consists of four main systems; the probe station cryostat, a vacuum system, cooling system, and a viewing apparatus. A photograph of the probe station with a magnified view of the sample stage and probes is shown in Fig. 2.2.

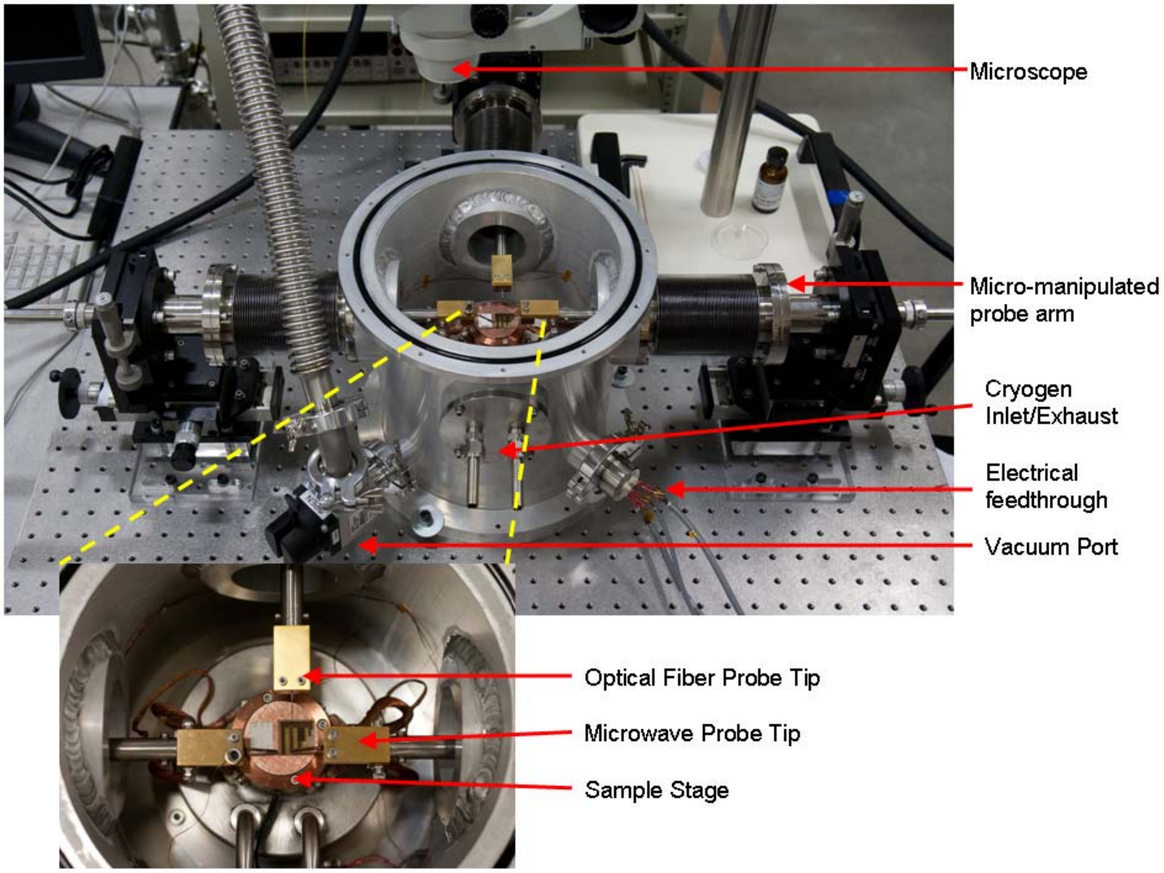

Figure 2.2 Photograph of probe station with magnified view of sample stage and probe tips

In order to view the wafers placed on the sample stage a Nikon SMZ660 stereomicroscope is used along with an articulating arm boom stand. This viewing system allows us to accurately place the probes at any location on the wafer. The movement of the probes is provided through the use of micromanipulators. Newport 426A series micromanipulators located outside the cryostat provide the movement for the probe arms which support the microwave probes. The probes can move across the entire sample stage area using stainless steel vacuum bellows to couple the micromanipulator flange to the flange on the cryostat.

2.1.1 Vacuum and Cryogenic Considerations

The main chamber of the probe station is manufactured with 6061 aluminum alloy. Four flanges are welded 90 degrees apart from each other on the sidewall of the cryostat chamber. These flanges serve as the ports for the probe arms to enter the cryostat and provide a vacuum seal with an o-ring. One of the flanges is used as a port for the cryogen inlet/outlet. Before cryogenic temperature can be achieved, the cryostat must be evacuated. The vacuum pump access is provided through the QF25 flange labeled ‘vacuum port’ in Fig. 2.2. The probe station can achieve a vacuum level of roughly $5x10^{-5}$ mbar after pumping for several hours with a turbo molecular and roughing pump setup.

As mentioned above, the cryogen inlet and exhaust is provided through one of the flanges on the side wall of the probe station. This port is shown in Fig. 2.3. The cryogen liquid flows through the stainless steel tubing into a sealed stainless steel reservoir inside the vacuum chamber. The stainless steel tubing is fastened to the flange on the probe station sidewall and to the stainless steel reservoir with Swagelok® tube fittings. These fittings use a stainless steel compression ferrule ensuring a vacuum tight seal at cryogenic temperatures. The cryogen reservoir is also welded to be vacuum tight such that it does not compromise the vacuum of the probe station chamber. The reservoir has a 2 inch diameter copper rod placed through the center of the top cover. The idea is to fill this reservoir with liquid cryogen, thereby cooling the copper rod which will serve of the cold stage for the probe station. The critical point in this setup is to provide a vacuum seal at cryogenic temperatures between the gold plated copper rod and the stainless steel cryogen reservoir.

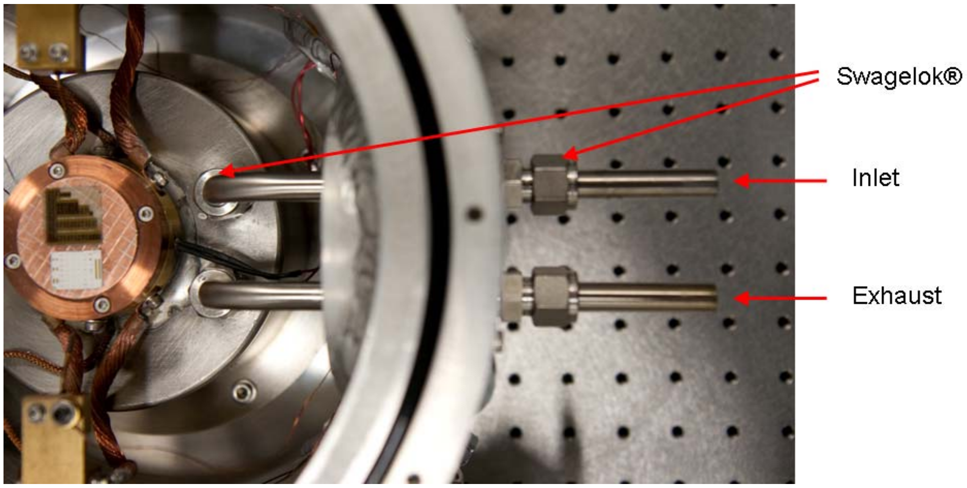

Figure 2.3 Ports for cryogen inlet/exhaust sealed with Swagelok® tube fittings.

Several options are available to join copper to stainless steel; brazing, soldering, and epoxy to name a few [17]. The main difference between brazing and soldering is that the melting temperature between the intermediary metal is much higher with brazing, typically 950°C. This is not useful for our application because the thin gold plated layer on the copper rod will delaminate at high temperatures, causing the cold stage to oxidize. Most epoxies can be cured at room temperature; however it must also maintain its integrity at cryogenic temperatures. Stycast 2850FT™ Catalyst #9 is a special glass filled epoxy which has an average thermal contraction matched to that of copper through the addition of low thermal contraction ceramic powder [17]. This lends itself for use in cryogenic applications where a joint with copper is needed. Several tests were performed to evaluate the performance of a copper to stainless steel joint. A test piece was made duplicating the exact joint geometry needed to affix the copper rod cold stage to the stainless steel reservoir. This test piece was thermally cycled several times from 77K to room temperature. It did not provide a reliable seal, as the vacuum performance slowly degraded after thermal cycling.

The options for a solder to join the cold stage to the stainless steel reservoir led to the selection of a "soft-silver solder" called Staybrite™. It is composed of 96%Sn-4%Ag, with a melting point of 221°C. At this temperature, the gold plating on the cooper rod will remain undamaged and yet still provide a high strength mechanical joint between the cold stage and the cryogen reservoir. An image of the Staybrite™ joint on the actual probe station is shown in Fig. 2.4.

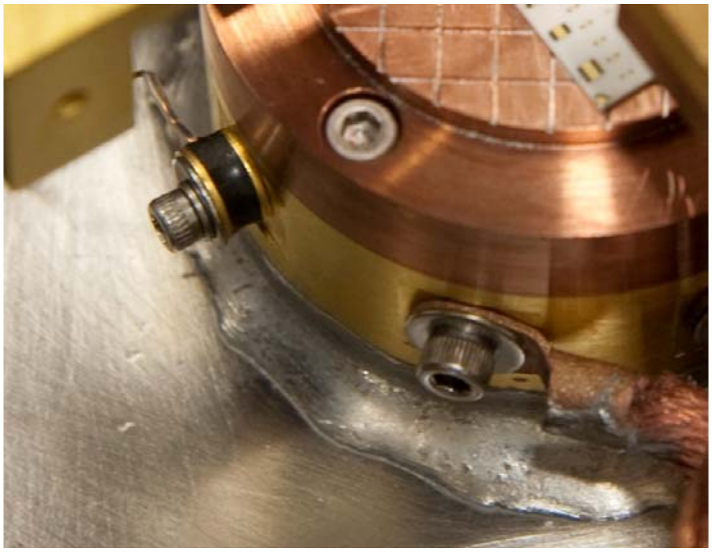

Figure 2.4 Staybrite™ joint between the gold plated cold stage and the stainless steel reservoir

2.1.2 Probe Station Cryogenic Performance

For proper operation of the probe station the sample stage along with the microwave probe tips must be cooled down to ensure reliable measurements of superconducting devices. It is imperative that the probes are sufficiently cooled such that they do not act as a heat load when they come in contact with the device under test. Several copper braids are attached from the cold stage to the probe holders, serving as a thermal anchor for the microwave probes to the sample stage. This can be seen in Fig. 2.5. The copper braids are screw tightened in Heli-Coil® inserted screw threads to ensure a tight, secure, and reliable thermal contact.

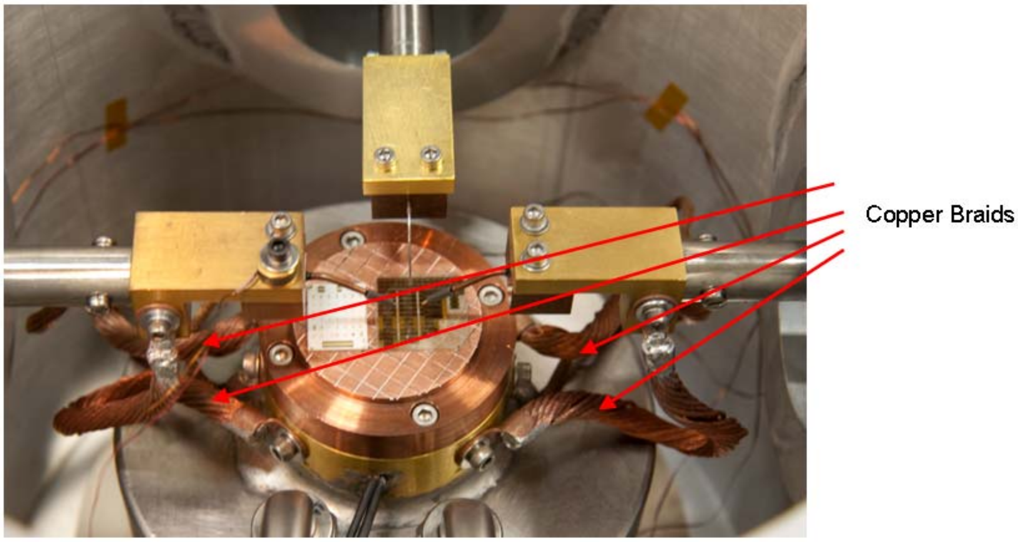

Figure 2.5 Copper Braids thermally anchoring microwave probes to the cold sample stage

The temperature curves for both the sample stage and the probes are shown in Fig. 2.6. Two silicon diode sensors are present in the system to monitor these temperatures, one on the sidewall of the sample stage, the other on the probe holder. The location of the temperature sensors is shown in Fig. 2.7. The sample stage reaches an equilibrium temperature of 77.5K when cooled with liquid nitrogen. It takes approximately 25 minutes to cool down the sample stage to liquid nitrogen temperature. The microwave probes require approximately one hour to achieve a steady state temperature of approximately 90K. This provides an appropriate platform to perform measurements on HTS devices at liquid nitrogen temperatures. A cartridge heater is also buried inside the sample stage and soldered in place with indium. The heater provides temperature control of the sample stage to within 0.1K stability.

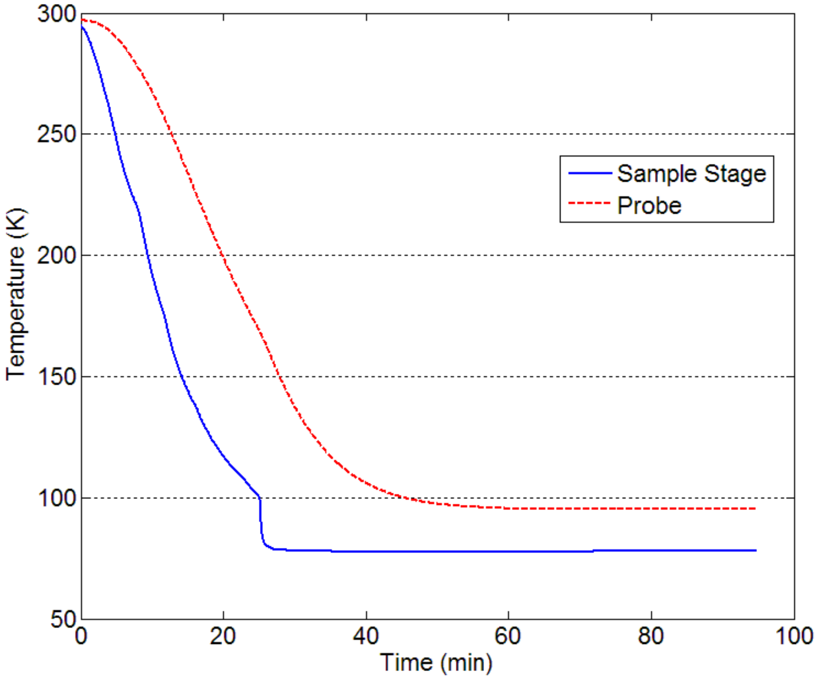

Figure 2.6 Temperature vs. time curves for the sample stage and microwave probes

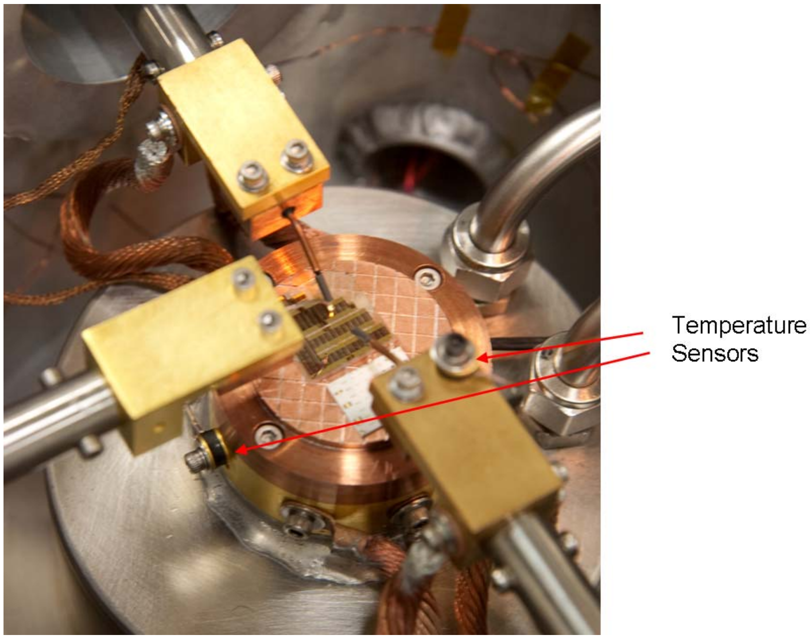

Figure 2.7 Locations of the temperature sensors in the probe station

2.1.3 Sample Stage Design and Operation

The sample stage is a crucial component of the cryostat as it is ultimately responsible for conducting heat away from the samples. Fig. 2.8 shows an image of the copper sample holder used in this probe station. It is designed to be modular such that samples can be mounted outside the cryostat and then placed inside the probe station. It is tightened to the cold stage with four screws into Heli-Coil® inserted screw threads. The large surface area contact between the two metals ensures a good thermal contact.

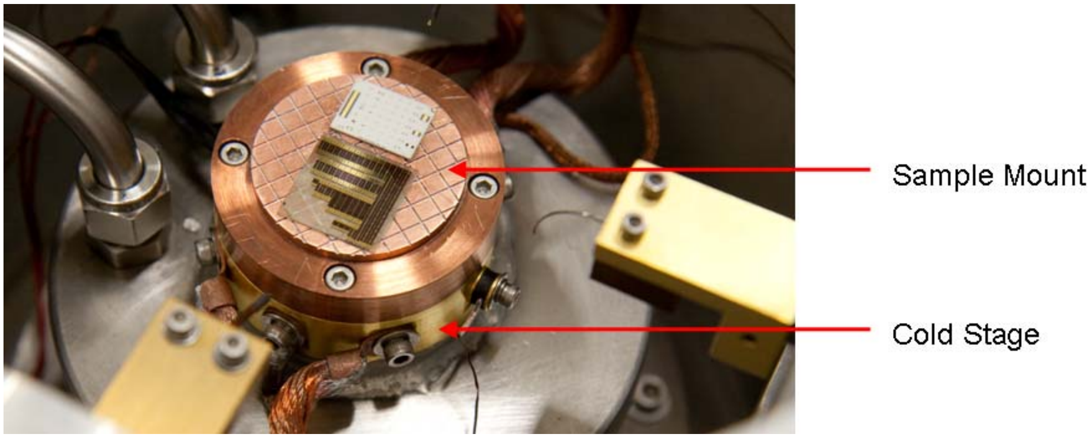

Figure 2.8 Sample mount and cold stage

Several options are available to mount wafers onto the sample stage. The critical factor is to provide a good thermal contact such that the wafer is sufficiently cooled. Apiezon® N Cryogenic High Vacuum Grease can be used to secure the wafer to the sample stage, however for a good thermal contact small wafer clips are needed to provide some mechanical force pressing the wafer and the sample mount together. This will limit the size of the wafer we can place on the sample mount and confine the area on the wafer which we can pattern devices to leave room for these sample clips. Silver pastes can be used to adhere the wafer to the sample mount and provide a good thermal contact. Several pastes were experimented with and are summarized in table 2.1. The "Leitsilber" Conductive Silver Cement from Ted Pella was selected as the most appropriate paste for this application. It provides good thermal conductivity, short drying times (approx. 30 min), and works at cryogenic temperatures. An additional advantage of this silver cement is that it readily dissolves in acetone making it easy to remove the wafer from the sample stage. The PELCO® High Performance Silver Paste works exceptionally well at cryogenic temperatures, however it is quite difficult to remove once cured. The SPI Supplies® silver pastes were found not to provide a reliable thermal contact at cryogenic temperatures.

Table 2.1 Silver paste manufacturers for mounting wafers to sample stage

Product	Manufacturer
"Leitsilber" Conductive Silver Cement	PELCO®
PELCO® High Performance Silver Paste	PELCO®
SPI Supplies® Brand Conductive Silver Paint	SPI Supplies®
SPI Flash-Dry™ Silver Paint	SPI Supplies®

As seen in Fig. 2.8, the surface of the sample mount has a hatched pattern machined onto the top face where the wafers are mounted. This hatch pattern serves several purposes. First, it provides channels for a solvent such as acetone to flow, dissolving the silver paste and making it quite easy to remove the wafers. Second, the hatch pattern creates channels for the air to escape when evacuating the chamber with the vacuum pumps. Air can get trapped during the process of securing the wafer to the sample mount with silver paste. If these channels where not present, the escaping air could shift the wafers around, even lifting the wafer off the sample mount surface creating a poor thermal contact.

2.2 PNA Calibration at Cryogenic Temperatures

To measure the microwave performance of our microwave photonic devices a network analyzer will be used to measure scattering parameters. The instrument used in this work is the Agilent 8364B PNA which covers a frequency range of 10MHz to 50GHz. A significant challenge in such measurements manifests itself in defining where the measurement system ends and where the device under test (DUT) begins. Regarding on wafer PNA measurements, this boundary is known as the reference plane, and ideally should be located at the tip of the microwave probes. Therefore the PNA must be calibrated to cancel out the effects of cables, probes, and certain internal characteristics of the PNA itself [18]. If performed incorrectly, calibration can introduce errors in measured data; hence it is imperative to attain an accurate, reliable, and repeatable calibration. For on wafer calibration, special calibration standards are used which most often consist of precision thin-film resistors, open and short circuit connections, and 50 ohm transmission lines. In some applications the standards can be fabricated directly on the DUT wafer.

By far the most common method for network analyzer calibration is the Short-Open-Load-Thru, or SOLT calibration. For a 2 port system, it consists of two 1 port Open-Short-Load calibrations and one 2 port Thru calibration. The SOLT standards are modeled as simple lumped elements. Therefore, the placement of the probes on the pads leading to the standards is critical, as it results in a significant change in the inductance value. This can be seen in Fig. 2.9. A deviation of 25µm between the probe tips on the calibration standard, significantly affects the measured behavior of the standard [18].

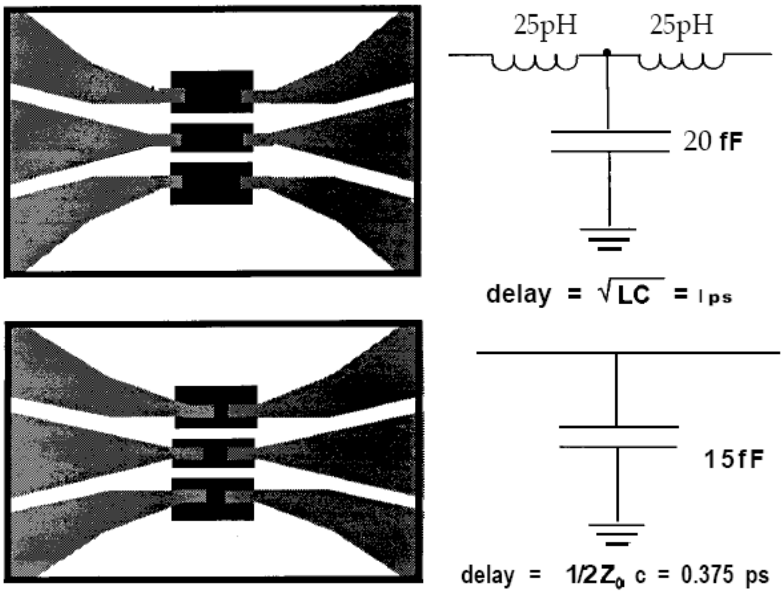

Figure 2.9 Improper probe placement causing a significant change in the measured response [18]

At cryogenic temperatures SOLT calibration is not recommended as the load value will drift due to its temperature coefficient. Other methods have been suggested, such as using an auxiliary chuck for the calibration substrate, which is thermally isolated and held at room temperature to perform SOLT calibration. This adds to the system complexity of the cryostat and is not very practical. Another calibration method, Thru-Reflect-Line or TRL, uses the characteristic impedance of a transmission line as the reference for calibration [18]. Therefore, this calibration method only depends on the geometry of the standards and not on a temperature dependent resistor. However, due to physical limitations of line lengths on the calibration substrate, it curbs the accuracy in the lower frequency range.

To attain an accurate calibration at cryogenic temperatures for the entire frequency span of interest, a modified calibration substrate was used from GGB Industries. By trimming the precision resistors on the CS-5 calibration substrate with a laser trimmer, we were able to attain a DC resistance of 50.05Ω at 77.5K. This provided an accurate and reliable platform to perform cryogenic on wafer calibration in the cryogenic microwave probe station.

2.3 Optical Fiber Probe

The objective of this work is to measure the behavior of superconducting microwave photonic and optoelectronic devices. Therefore it is necessary to introduce a laser source into the probe station to excite the devices with light. One of the probe arms entering the probe station is adopted to serve this purpose. An image of the fiber optic probe tip is shown in Fig. 2.10. A Corning® SMF28 optical fiber is passed through the probe arm, much in the same way a coax cable is passed through the microwave probe arms. A new probe tip is machined to guide the optical fiber such that it is perpendicular to the sample stage surface. The bending radius of the fiber optic tip is kept large enough such that it does not incur significant attenuation due to bending, less than 0.05dB [19]. The optical fiber tip can be positioned with micro-manipulators to adjust its position to an appropriate location on the wafer.

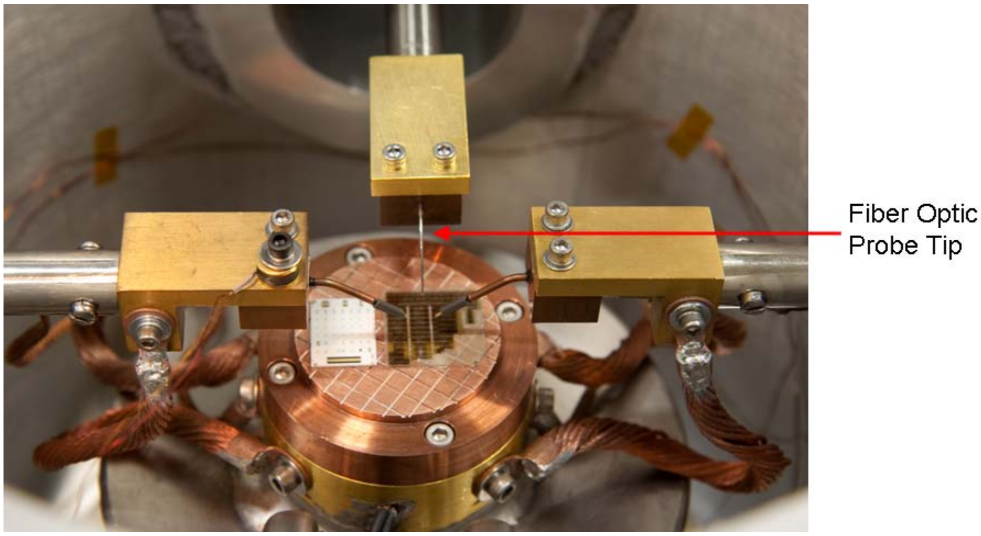

Figure 2.10 Fiber optic probe tip for photo-excitation of HTS devices

Chapter 3

Superconducting Coplanar Waveguide (CPW)

The superconducting coplanar waveguide will serve as the groundwork for all the superconducting microwave photonic devices. Therefore, it is imperative to have a transmission line design with exceptional performance. This section will introduce the HTS film used in our designs, followed by the design methodology behind the CPW with a comparison to the measurements data.

3.1 Sample Fabrication and Characterization

3.1.1 The Material: YBCO Thin Films

In this work, the HTS samples used to realize the devices are $YBa_2Cu_3O_{7-\delta}$ (YBCO) thin films. YBCO was discovered in 1987 as the first HTS with a T_c above the liquid nitrogen temperature [20]. YBCO is a typical HTS with a layered structure. One of the common features in most HTSs is the presence of copper oxide (Cu-O) planes. For this reason, HTSs are sometimes referred to as copper oxide superconductors, cuprate superconductors, or high T_c oxides. Fig. 3.1 shows the structure of the YBCO unit cell [21]. The structure crystallizes as a tetragonal at high temperatures, but converts by oxygen ordering to an orthorhombic form when cooled [22], [23]. The Cu-O planes are an important feature of HTSs. It is commonly believed that superconductivity occurs within these Cu-O planes, making the conductivity of the film anisotropic. Having such a complex structure, it is no surprise that the actual nature of superconductivity in HTSs remains to be a mystery.

3.1.2 Film Deposition by Reactive Thermal Co-evaporation

There are several different methods available for YBCO deposition: sputtering [24], pulsed laser deposition [25], molecular beam epitaxy [26], and chemical vapour deposition [27]. YBCO films used in this work were prepared by THEVA GmbH by reactive thermal co-evaporation. Theva GmbH has developed this process to perfection, yielding high quality films providing us with high performance, reliable YBCO wafers.

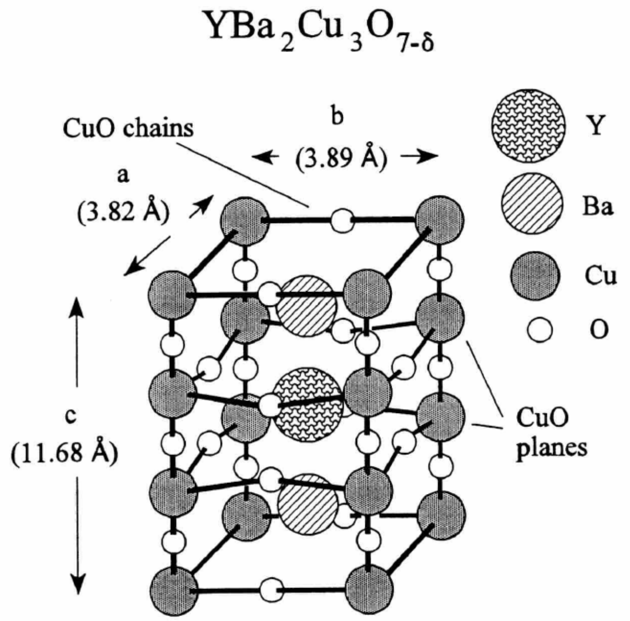

Figure 3.1 Unit cell of YBCO illustrating the location of the Cu-O planes [21]

100 nm thick YBCO films have been deposited on (001) $LaAlO_3$ (LAO) substrates by reactive thermal co-evaporation at a temperature of 680°C. The composition of the film has been optimized to get a very smooth film surface with good superconducting properties. Surface roughness is less than 5 nm as measured by AFM. Transition temperature and critical current density is 86.9 K and 4 MA/cm^2, respectively. After cool-down in an oxygen atmosphere, a 200 nm gold layer was deposited in situ to make good contact with the superconductor. The resistance vs. temperature curve for this film is shown in Fig 3.2, and an SEM of the film is shown in Fig 3.3 illustrating the smooth surface.

A schematic of the deposition process is shown in Fig. 3.4 [28]. The three metals yttrium, barium, and copper, are evaporated from resistively heated boats inside a vacuum deposition chamber. The rate of evaporation for each metal is individually controlled by a quartz crystal monitor to maintain the accurate ratio during deposition. The YBCO film is formed in an atmosphere with an oxygen partial pressure of 10^{-2} mbar. At the same time, the chamber pressure must be at least 10^{-5} mbar to ensure the metal vapors reach the substrates ballistically. Therefore, the wafers are mounted on a rotating disc such that they pass through both regions, the small oxygen pocket zone and the zone containing the metal vapors. With a rotation frequency of 5Hz, the metal atoms condense on the substrate surface and then oxidize in the oxygen pocket forming YBCO. The substrate is also heated to 680°C during deposition to form the YBCO thin film [29].

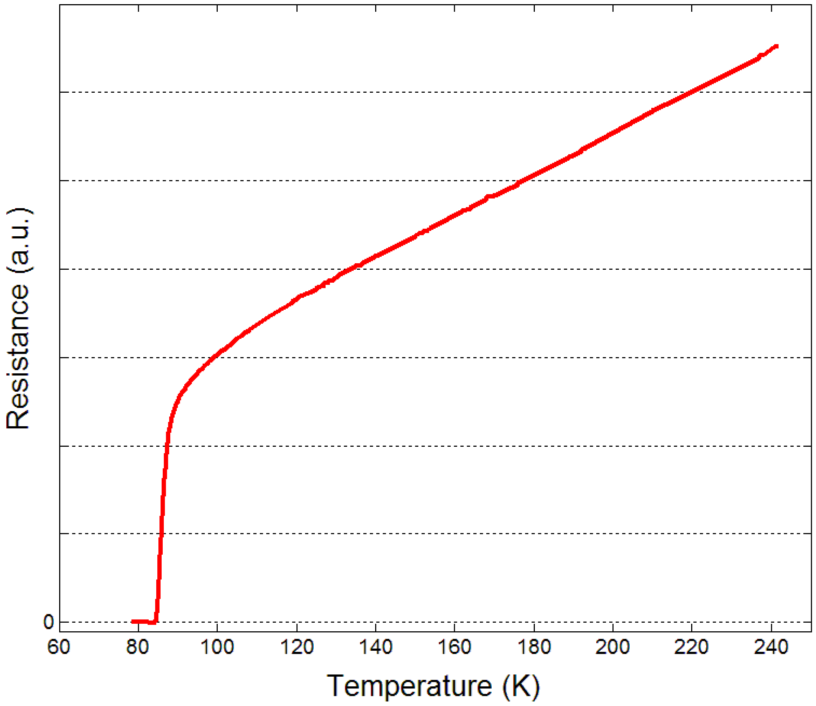

Figure 3.2 Resistance vs. temperature for 100nm YBCO thin film from Theva

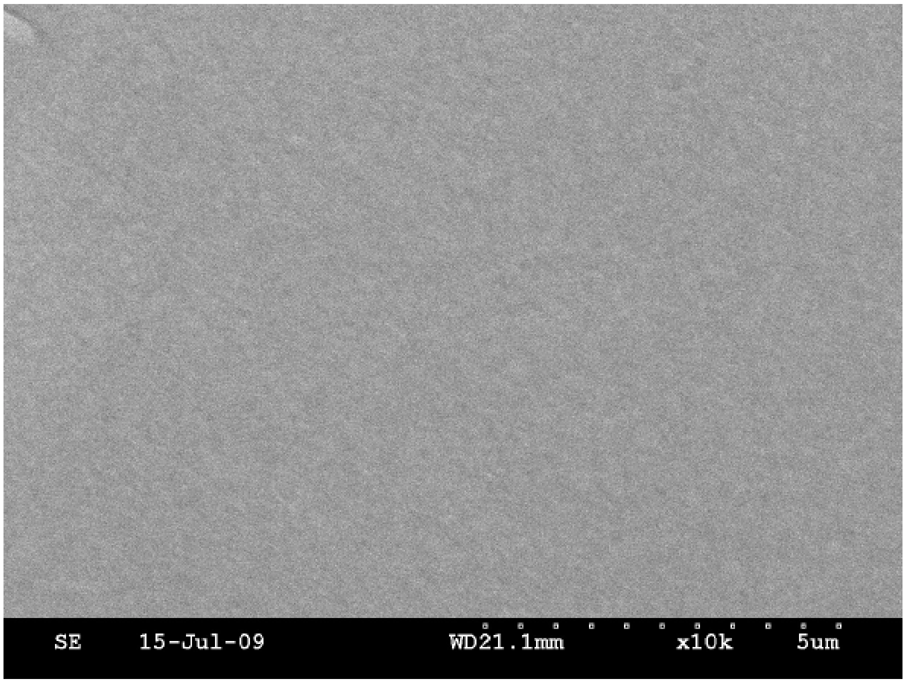

Figure 3.3 SEM of YBCO film on 20mm x 20mm LAO substrate illustrating smooth surface

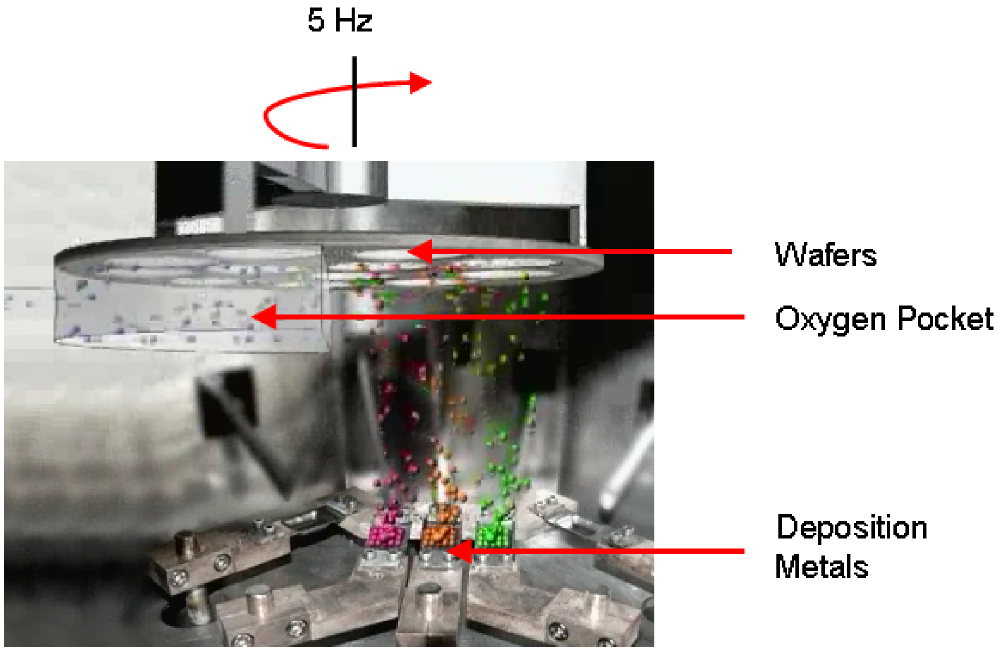

Figure 3.4 Deposition schematic for thermal co-evaporation combined with oxygen pocket [28]

3.1.3 Device Patterning

Device patterning using YBCO thin films must be done with care. To achieve small device dimensions in the micrometer range, typical wet etch photolithography cannot be employed. With the use of argon ion milling, small feature sizes can be patterned suitable for our microwave photonic devices. The process of argon ion milling is straightforward. Argon ions are bombarded on a sample specimen through a mask, etching the desired structure on the substrate surface. The mask can be a metal mask, or a photo resist mask developed on the substrate surface. A schematic of the process is shown in Fig. 3.5. Due to the aggressive nature of film removal, ion milling tends to raise the temperature of the substrate by a considerable amount. This is not suitable for YBCO as increasing the temperature of the film causes oxygen to diffuse out of the film destroying the superconducting properties [31], [32]. Fig 3.6 shows the strong dependence of the critical temperature to the ratio of oxygen present in the YBCO thin film. Consequently, a cooling mechanism must be utilized to ensure the temperature of the YBCO film does not significantly increase during etching.

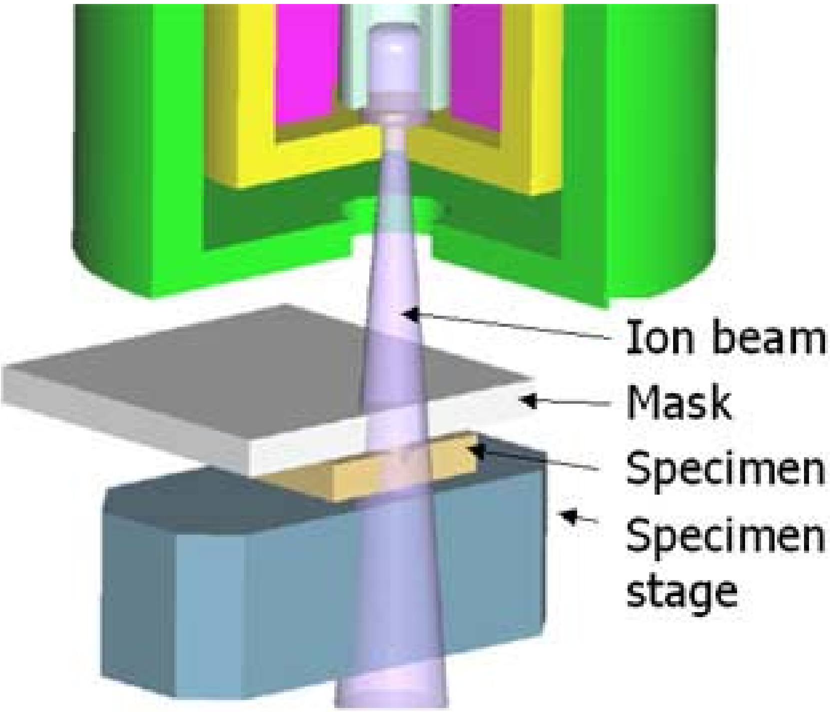

Figure 3.5 Schematic of argon ion milling [30]

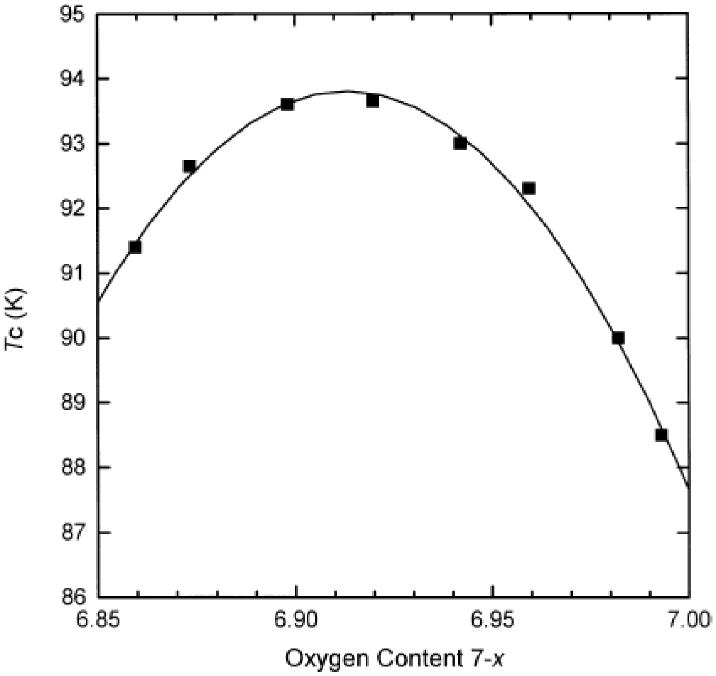

Figure 3.6 Relationship of T_c to oxygen content in $YBa_2Cu_3O_{7-x}$ [32]

The device patterning was done by Star Cryoelectronics in NM, US. Some of the fabrication details are proprietary to Star Cryoelectronics; however a general summary of the process is described. The YBCO/Au films deposited on 2 cm x 2 cm LAO substrates are patterned using a resist mask and argon ion milling. To cool the films during milling, the substrates are clamped to an aluminum puck filled with a salt that undergoes a solid-to-liquid phase change at 38°C. The salt keeps the temperature of the puck at the melting temperature during the milling process. To improve thermal contact with the chuck, the substrates are greased to the chuck using a small amount of thermal grease. After milling through the YBCO/Au film stack, the resist mask is stripped, and a new resist mask is prepared to pattern the top Au layer to form the contact pads of the devices. The exposed Au is etched using a potassium iodide (KI) solution. After etching the Au, the resist mask is stripped.

An image of the GDSII layout file to generate the necessary chromium masks for fabrication of the YBCO designs is shown in Fig. 3.7. The brown color represents the 100nm YBCO layer, and the yellow sections represent the areas covered with 200nm of gold to serve as device contacts. Originally the mask was designed for a 2inch LAO wafer which would be diced in four quarters represented by the blue lines in Fig. 3.7. Subsequently, the mask was patterned on four 2cm x 2cm square wafers, 500µm thick. All designs are made to be compatible with the 200µm pitch microwave probes used in our cryogenic microwave photonic probe station.

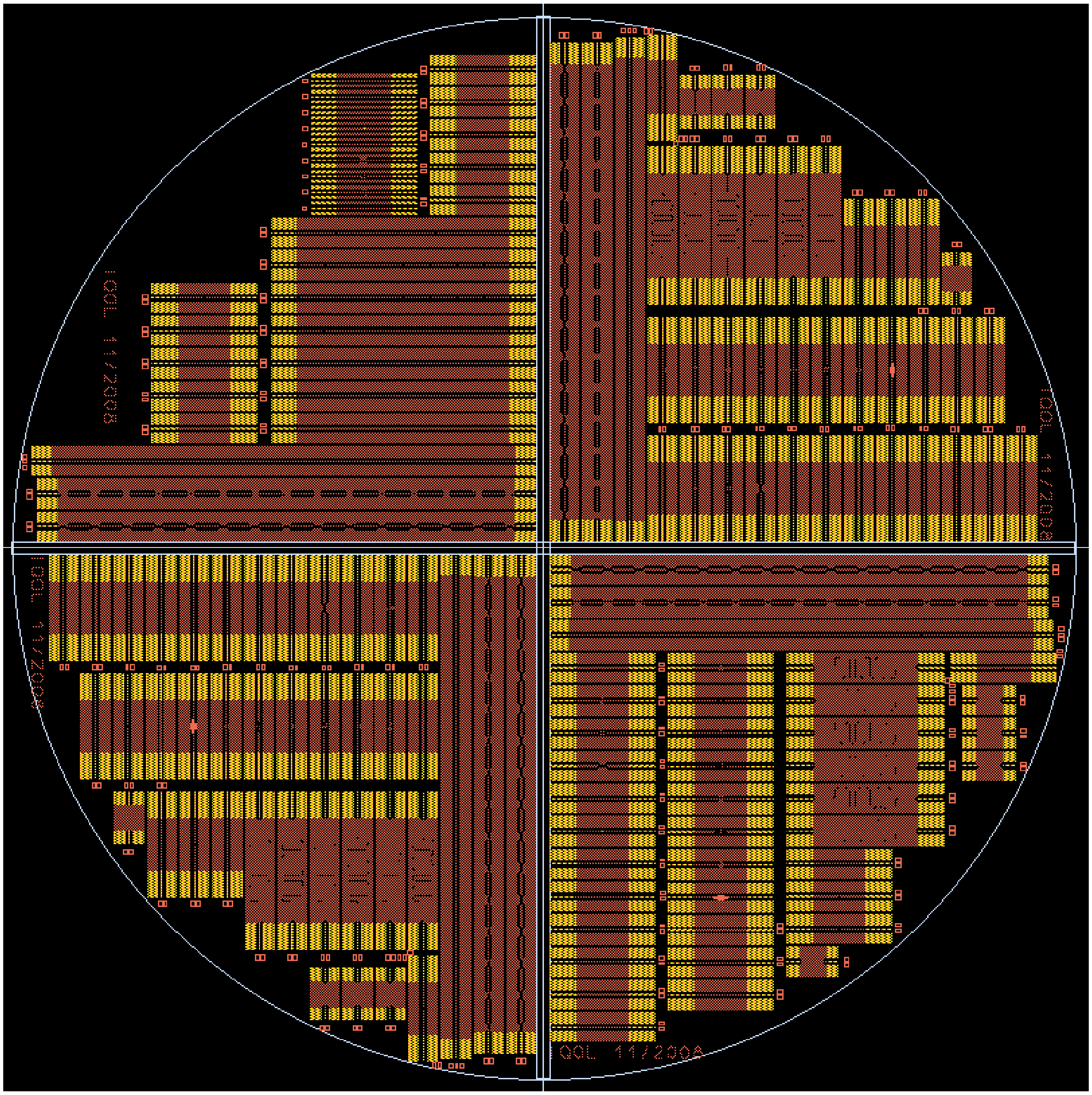

Figure 3.7 GDSII layout design for YBCO/Au film device patterning

3.2 CPW Design and Measurement

It is a well accepted fact that the use of superconductors enhances the performance of TEM transmission lines. Superconducting transmission lines have two key features distinguishing them from normal metal transmission lines; they are ultra-low loss and have ultra-low dispersion. Since the conductivity in superconductors is due to Cooper pairs which do not exhibit scattering from the lattice, a very small resistance is observed. Superconductors are non-dispersive in nature due to the penetration depth of the electromagnetic field through the superconductor being frequency independent, as opposed to the skin depth in normal metals [4], [33], [34]. Superconducting transmission lines also have another intrinsic property known as kinetic inductance, which is added in series with the transmission line. This added inductance is contributed by the inertial mass of the Cooper pairs in a superconducting material. Therefore a superconducting transmission line is well suited for applications in ultra high performance microwave and optoelectronic devices [35], [36].

A transmission line is usually referred to as a waveguide if it can support one propagation mode. If the principle mode is a TEM mode, the voltage and current can be defined within the waveguide and distributed circuit theory can be utilized to analyze the TL [34]. To support an ideal TEM mode a transmission line must satisfy the following six conditions:

1. The number of conductors should be two or greater [37]
2. Transmission line conductors should be perfect electric conductors (lossless)
3. Media surrounding the TL should be homogeneous [38]
4. Transverse dimension with respect to the waveguide must be small compared to the wavelength
5. Frequency within the waveguide must be low enough not to excite higher order modes [34]
6. The waveguide must be kept uniform along the direction of propagation

Therefore the realization of a true TEM waveguide is quite difficult in practice. For our purpose we have chosen to use the coplanar waveguide (CPW) transmission line (TL). This is well suited for our application as it is a planar structure (the entire device is on one side of the wafer). There are three distinctive conductors, one signal conductor or center strip, and two ground strips on either side of the center strip at an equal distance, all on a dielectric substrate. The CPW structure fabricated on the wafer described in section 3.1 is illustrated in Fig. 3.8. The center strip dimension, the gap spacing, the film thickness and the dielectric height are denoted by (s), (w), (t), and (h) respectively. This structure lends itself for on wafer probing with high frequency microwave probes, and accommodates for easy optical excitation of the device from the top side of the wafer.

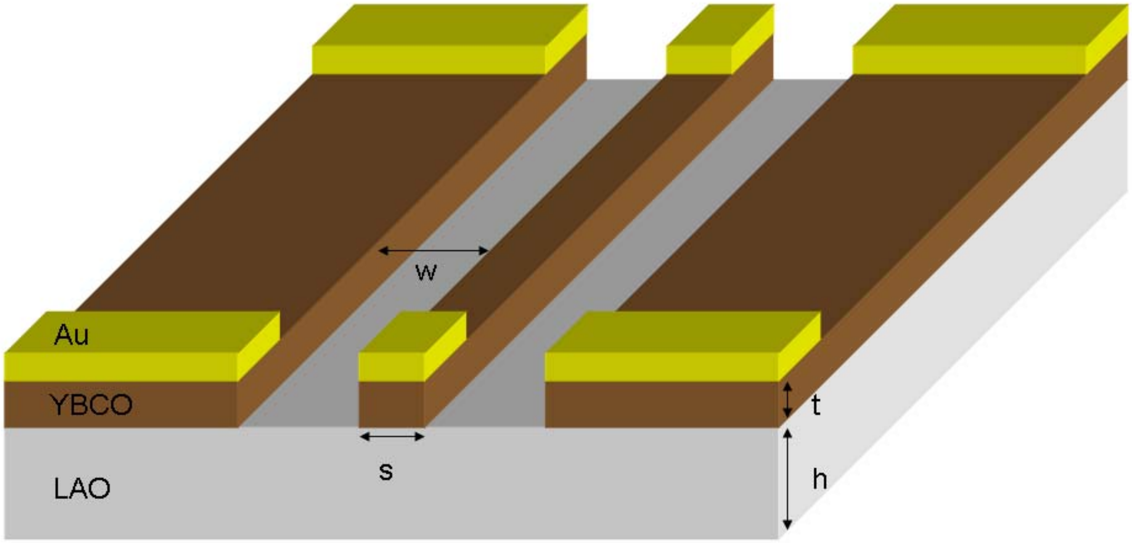

Figure 3.8 HTS CPW transmission line

The dominant mode of propagation in a CPW resembles a quasi-TEM mode, but at higher frequencies becomes non-TEM. However, in many microwave applications the dimensions of the CPW are small enough to assume quasi-TEM, and we analyze the structure as such [38].

3.2.1 CPW Design Method

The objective of this section is to present a design methodology for the CPW transmission line structure. Using the concept of surface impedance associated with a superconductor and conventional CPW design techniques, a set of closed-form equations are presented to design a CPW with desired parameters. An equivalent circuit model for a superconducting transmission line is shown in Fig. 3.9. Note the addition of an extra inductance labeled kinetic inductance to model the effect of the Cooper-pairs. By solving for the circuit parameters in Fig. 3.9, the superconducting transmission line can be fully characterized.

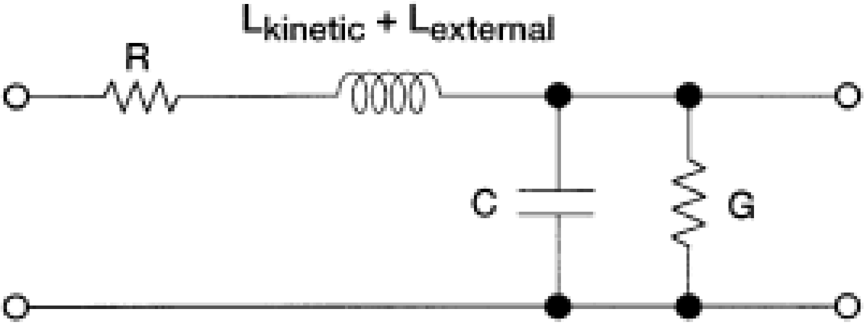

Figure 3.9 Lumped element equivalent circuit model for a superconducting TL [38]

The geometrical dimensions of a CPW are illustrated in Fig. 3.8. The shunt capacitance and the shunt conductance are not affected by the presence of a superconductor; therefore general relations for a CPW can be used. The capacitance per unit length is given by

$$C = 2\varepsilon_0(\varepsilon_{rd} - 1)\frac{K(k_1)}{K(k_1^{'})} + 4\varepsilon_0\frac{K(k_0)}{K(k_0^{'})} \tag{3.1}$$

where ε_0 and ε_{rd} represent the permittivity of free space, and the dielectric constant of the substrate material respectively [39]. $K(k_0)$ is the complete elliptical integral of the first kind and the parameters $k_0, k_0^{'}, k_1$ and $k_1^{'}$ are given by

$$k_0 = \frac{s}{s+2w} \tag{3.2}$$

$$k_0' = \sqrt{1-k_0^2} \tag{3.3}$$

$$k_1 = \frac{\sinh\left(\frac{\pi s}{4h}\right)}{\sinh\left[\frac{\pi(s+2w)}{4h}\right]} \tag{3.4}$$

$$k_1' = \sqrt{1-k_1^2} \tag{3.5}$$

In an inhomogeneous dielectric structure, such as the CPW, the dielectric constant varies with position. In such a case, the supporting wave in the waveguide is not TEM. However, for practical purposes, it is useful to assume an ‘effective dielectric constant’ calculated from the geometry of the dielectrics in the surrounding medium. This definition allows for the analysis of the propagation in the CPW as quasi-TEM. The following expressions give the 'filling factor' and the 'effective dielectric constant' for a CPW transmission line, respectively [40].

$$q = \frac{1}{2}\frac{K(k_1)K(k_0')}{K(k_1')K(k_0)} \tag{3.6}$$

$$\varepsilon_{ref}(0) = 1 + q(\varepsilon_{rd} - 1) \tag{3.7}$$

where $\varepsilon_{ref}(0)$ is the effective dielectric constant for a zero thickness conductor at DC. The effect of the finite conductor thickness on $\varepsilon_{ref}(0)$ can be modeled by the following empirical relation take from [40].

$$\varepsilon_{ref}^{t}(0) = \varepsilon_{ref}(0) - \frac{0.7\left[\varepsilon_{ref}(0) - 1\right]\frac{t}{w}}{\frac{K(k_0)}{K'(k_0)} + 0.7\frac{t}{w}} \tag{3.8}$$

The frequency dependence on the effective dielectric constant is denoted by $\varepsilon_{ref}^{t}(f)$ and can be expressed in a closed-form expression, as presented in [41].

$$\sqrt{\varepsilon_{ref}^{t}(f)} = \sqrt{\varepsilon_{ref}^{t}(0)} + \frac{\sqrt{\varepsilon_{rd}} - \sqrt{\varepsilon_{ref}^{t}(0)}}{1 + g \times \left(\frac{f}{f_{TE}}\right)^{-1.8}} \tag{3.9}$$

$$g = e^{u \times \ln\left(\frac{s}{w}\right) + v} \tag{3.10}$$

$$f_{TE} = \frac{c_0}{4h\sqrt{\varepsilon_{rd} - 1}} \tag{3.11}$$

$$u = 0.54 - 0.64p + 0.015p^2 \tag{3.12}$$

$$v = 0.43 - 0.86p + 0.54p^2 \tag{3.13}$$

$$p = \ln\left(\frac{s}{h}\right) \tag{3.14}$$

c_0 is the speed of light in free space. The error in this model is suggested to be about 5% when 0.1 < w/h < 5, 1.5 < ε_{rd} < 50, 0.1 < s/w < 5 and $0 < \left(\frac{f}{f_{TE}}\right) < 10$.

When considering the case of dielectric loss, the shunt conductance of the TL can be model by

$$G = \omega C q \tan\delta \, . \tag{3.15}$$

where q is defined as the filling factor, ω is the frequency, and $\tan\delta$ is tangent loss of the dielectric material [34].

Referring back to the circuit model for the CPW in Fig. 3.9, the total inductance of the line is divided into two parts. The internal inductance or kinetic inductance of the transmission line, which represents the magnetic energy stored inside the conductors, and external inductance which represents the magnetic energy stored external to the conductors. The kinetic inductance arises from the inertia of the Cooper-pairs in the superconductor, and the external inductance originates from the flux linkage [39]. The kinetic inductance per unit length for a superconducting CPW is described in [42], [43] and [39] by using the conformal mapping technique. The contribution of the center signal strip and ground planes can be written explicitly as follows

$$L_{kin1} = \frac{\mu_0 \lambda_L C}{4ADK(k_0)} \times \frac{1.7}{\sinh\left(\frac{t}{2\lambda_L}\right)} \tag{3.16}$$

$$L_{kin2} = \frac{\mu_0 \lambda_L C}{4ADK(k_0)} \times \frac{0.4}{\sqrt{\left[\left(\frac{B}{A}\right)^2 - 1\right]\left[1 - \left(\frac{B}{D}\right)^2\right]}} \tag{3.17}$$

$$A = -\frac{t}{\pi} + \frac{1}{2}\sqrt{\left(\frac{2t}{\pi}\right)^2 + s^2} \tag{3.18}$$

$$B = \frac{s^2}{4A} \tag{3.19}$$

$$C = B - \frac{t}{\pi} + \sqrt{\left(\frac{t}{\pi}\right)^2 + w^2} \tag{3.20}$$

$$D = \frac{2t}{\pi} + C \quad . \tag{3.21}$$

Similar to the capacitance of the transmission line, the external inductance is independent of the conductor material. As a result, it is acceptable to calculate the external inductance for the case of a perfect electric conductor, and then applying the result to the superconducting transmission line circuit model. First we obtain the characteristic impedance of the transmission line, followed by the general relation to obtain the external inductance per unit length [39].

$$Z_0 = \frac{30\pi}{\sqrt{\varepsilon_{ref}^t}} \frac{k(k_0^{'})}{k(k_0)} \tag{3.22}$$

$$L_{ext} = Z_0^2 C \quad . \tag{3.23}$$

When the conductors of a CPW are not assumed to be perfect electric conductors, the concept of surface impedance is helpful to define the boundary conditions of the transmission line [34]. The surface impedance of a superconductor is given by a complex number with a positive imaginary component. The real component of the surface impedance represents the loss in the transmission line, modeled by the series resistance seen in Fig. 3.9. The positive imaginary component represents the kinetic inductance of the superconducting transmission line. The surface impedance of a superconducting plate can be found by the following relations

$$R_{s,sc}^t = \frac{1}{\delta_{sc}\sigma_n}\left(\frac{\lambda_L}{\delta_{sc}}\right)^3 \times \frac{\sinh\left(\frac{2t}{\lambda_L}\right) + \left(\frac{\delta_{sc}}{\lambda_L}\right)^2 \sin\left(\frac{2t\lambda_L}{\delta_{sc}^2}\right)}{\sinh^2\left(\frac{t}{\lambda_L}\right) + \sin^2\left(\frac{t\lambda_L}{\delta_{sc}^2}\right)} \tag{3.24}$$

$$X_{s,sc}^{\,t} = \frac{1}{2}\omega\mu_0\lambda_L \frac{\sinh\left(\frac{2t}{\lambda_L}\right) - \left(\frac{\lambda_L}{\delta_{sc}}\right)^2 \sin\left(\frac{2t\lambda_L}{\delta_{sc}^2}\right)}{\sinh^2\left(\frac{t}{\lambda_L}\right) + \sin^2\left(\frac{t\lambda_L}{\delta_{sc}^2}\right)} \tag{3.25}$$

where $R_{s,sc}^t$ and $X_{s,sc}^{\,t}$ represent the real and imaginary components of the surface impedance for a superconducting film respectively. λ_L, t, δ_{sc}, and σ_n represent the London penetration depth of a superconductor, the film thickness, the skin depth of the superconductor in the normal channel, and the conductivity of the normal channel of a superconductor [34]. The relations for the above parameters are given below.

$$\sigma_n(T) = \begin{cases} \sigma_0 & T \geq T_c \\ \sigma_0 \left(\dfrac{T}{T_c} \right)^{\gamma} & T \leq T_c \end{cases} \tag{3.26}$$

$$\lambda_L(T) = \begin{cases} \infty & T \geq T_c \\ \dfrac{\lambda_L(0)}{\sqrt{1 - \left(\dfrac{T}{T_c} \right)^{\gamma}}} & T \leq T_c \end{cases} \tag{3.27}$$

$$\delta_{sc}(\omega, T) = \sqrt{\frac{2}{\omega \mu_0 \sigma_n(T)}} \tag{3.28}$$

where σ_0 is the DC conductivity of the superconductor just above the critical temperature, and $\lambda_L(0)$ is the penetration depth at zero temperature. The exponent γ is a phenomenogical parameter which is typically 2 for HTS and 4 for LTS [44]. Note that δ_{sc}, skin depth of the superconductor in the normal channel, is just a name given to the expression in 3.28, it is not a material parameter.

After obtaining the surface impedance, the stored-time averaged magnetic energy and power loss per unit length can be calculated. This energy must be identical to its equivalent circuit theory model; therefore the following equation can be used to find the series kinetic inductance or series resistance in the transmission line model, where R_{sc} represents the series resistance of the superconductor plate [34].

$$\frac{R_{sc}}{R_{s,sc}^{t}} = \frac{\omega L_{kin}}{X_{s,sc}^{t}} \tag{3.29}$$

We have now obtained all the circuit model parameters for a superconducting CPW transmission line. All other properties of the transmission line can easily be extracted from these parameters. In order to design a CPW with YBCO on an LAO substrate, the following material parameters are needed and summarized in Table 3.1. These properties are sample dependent; nevertheless typical values are taken from the following sources [44], [45].

Table 3.1 Typical phenomenological parameters of YBCO thin films

Description	Value
Critical Temperature (T_c)	86.9K
Normal Conductivity @ T = T_c (σ)	1.7 x 10^7 Ωm^{-1}
London Penetration Depth (λ_L)	150nm
Relaxation time (τ_{tr})	3.57 x 10^{-15}sec
Exponent (γ)	2

The dielectric constant (ε_r) for LAO is taken to be 23.7.

3.2.2 The Experiment: Superconducting CPW Transmission Lines

In the previous section we have presented a set of closed-form equations to design HTS CPW transmission lines. In this section we will use the results obtained from these closed form equations to fabricate real CPWs from YBCO. The measurement data will be analyzed to ensure the results coincide with the theory. CPWs of varying dimensions were fabricated to characterize the robustness of the design. All CPWs are designed to be 50Ω, with dimensions such that they can be probed by the 200µm pitch microwave probes used in the probe station described in section 2. Five CPWs, 4mm in length, were designed with varying gap distances (94µm, 97µm, 100µm, 103µm and 107µm) keeping the center strip constant at 60µm. All S-parameter measurements are done with the Agilent 8364B PNA, and calibrated by the method describe in section 2.2. $|S_{11}|$ and $|S_{21}|$ for all five CPWs with varying gap spacing are shown in Fig.3.10 and Fig.3.11 respectively.

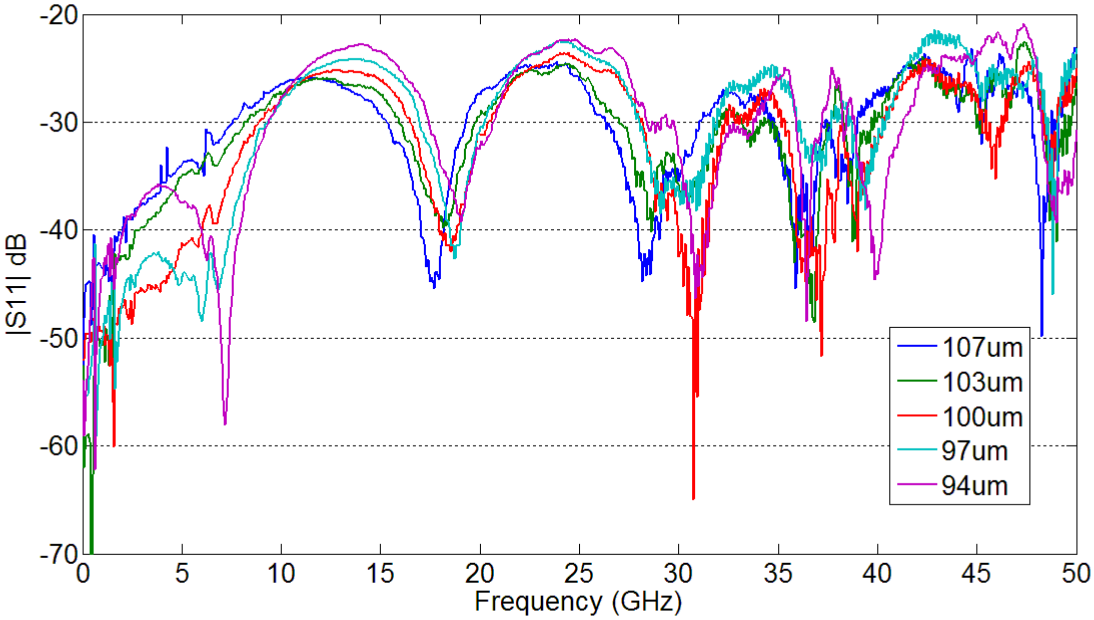

Figure 3.10 Magnitude of S_{11} for HTS CPWs with varying gap spacing

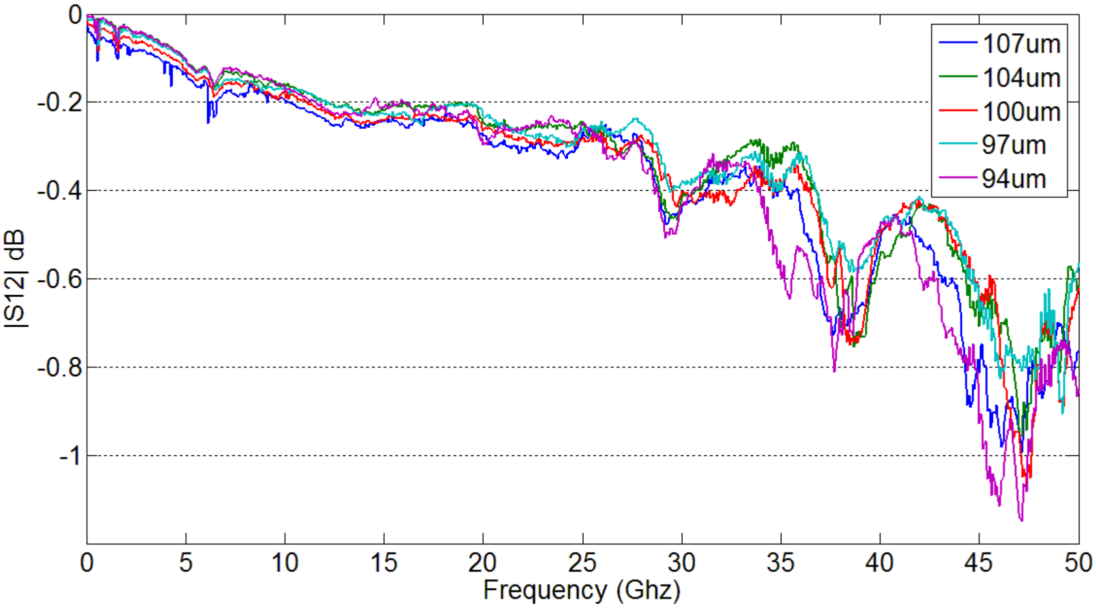

Figure 3.11 Magnitude of S_{12} for HTS CPWs with varying gap spacing

It can be seen from Fig 3.10 that the 107μm gap spacing TL exhibits the best return loss. Towards the higher frequencies the measurement data seems less consistent as we approach the limit of our measurement equipment, and parasitic effects become more pronounced.

The insertion loss of the TLs can be seen in Fig. 3.11. All the TLs appear to have attenuation within the same range. This is expected since the signal trace width is not varying and the losses should be approximately equivalent. The attenuation per millimeter for the CPWs at selected frequencies is summarized in table 3.2.

Table 3.2 Measured attenuation constants for YBCO CPW transmission lines

Film thickness (t)	Slot Width (g)	Center Strip Width (s)	Measured Attenuation Constant (dB/mm)					
			1 GHz	5GHz	10GHz	20GHz	40GHz	50GHz
100nm	107um	60um	0.015	0.033	0.049	0.069	0.129	0.192
	103um		0.004	0.025	0.041	0.062	0.137	0.153
	100um		0.009	0.031	0.046	0.065	0.125	0.155
	97um		0.005	0.027	0.042	0.057	0.121	0.142
	94um		0.003	0.026	0.043	0.074	0.121	0.211

It is evident the attenuation between the CPWs are quite close. The minor difference of several hundredths of a dB can be attributed to the contacts the probes make with the gold pads. It is difficult to produce the exact same contact with the microwave probes for each measurement. Slight differences in the pressure applied with the probes when contacting the device will inherently affect the measured data. Also, by contacting the same gold pad several times, the surface of the gold gets scratched and reduces the quality of the contact. Nevertheless, this difference is only several hundredths of a dB per mm, and does not have a considerable effect on the device performance.

The CPW structure chosen as the basis for all the microwave photonic devices is the 107μm gap spacing CPW. It provides the best match to 50Ω as seen from the $|S_{11}|$ measurements, while having an excellent attenuation constant throughout the entire frequency range. ADS momentum was used to simulate the 107μm gap spacing CPW. $|S_{11}|$ and $|S_{21}|$ simulation results with overlays of the measured data are shown in Fig. 3.12 and Fig. 3.13 respectively. We observe excellent agreeance between the measured data and the simulation.

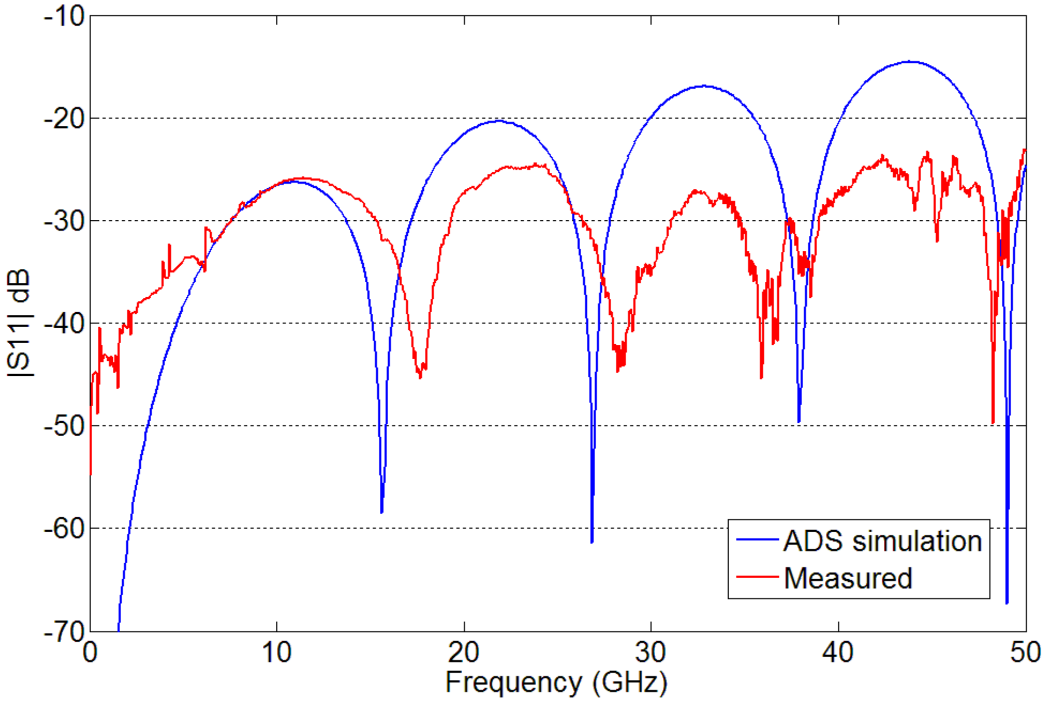

Figure 3.12 Magnitude of S_{11} measured vs. ADS simulation for HTS CPW

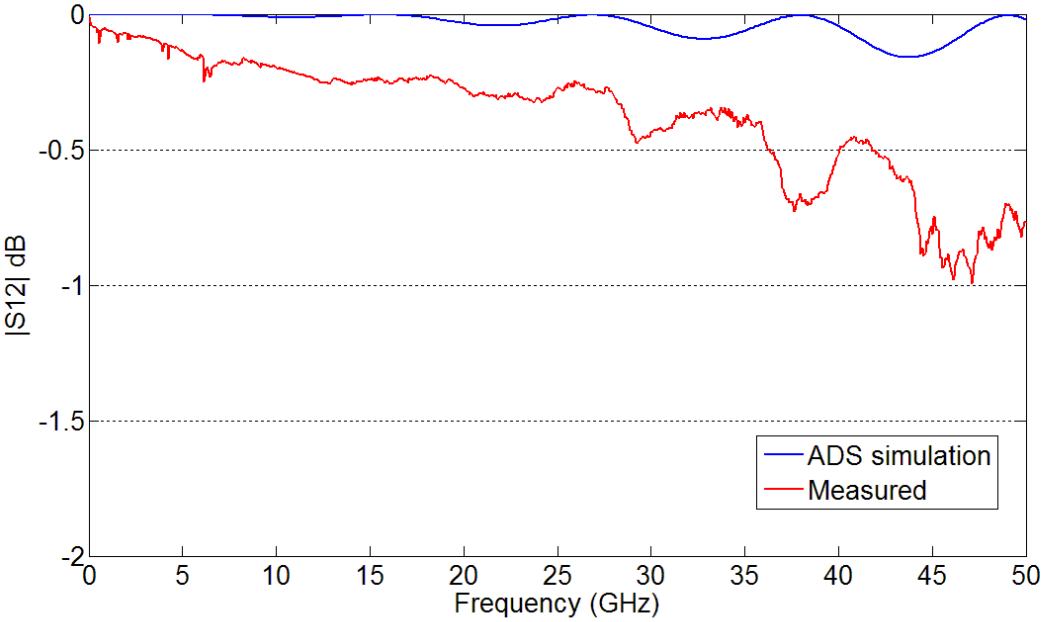

Figure 3.13 Magnitude of S_{12} measured vs. ADS simulation for HTS CPW

The next objective is to extract the circuit parameters from the actual measured s-parameters for the 107μm gap CPW, and compare them with the results obtained from the closed-form expressions in section 3.2.1. First, the propagation constant and the attenuation constant are obtained from the following relations [46].

$$S_{21} = |S_{21}|e^{j\varphi(S_{21})} = e^{-\alpha\ell}e^{-j\beta\ell} \tag{3.30}$$

$$\beta = -\varphi^{unwrapped}\left(S_{21}\right)/\,\ell + \xi \tag{3.31}$$

$$\alpha = -\ln|S_{21}|/\,\ell \tag{3.32}$$

where ℓ is total length of the transmission line and ξ is the phase offset from the unknown unwrapped phase. The computation of α is straightforward; however β requires two other considerations. First, due to the periodicity of the complex exponential function, the phase of S_{21} generally appears as a curve varying between –π and π with respect to frequency. However β is a continuous function with frequency, so it is necessary to unwrap the phase to restore the continuity of β. Hence, by "unwrapping", we mean to connect the discontinuous segments in the phase that occur at – π and π. Second, the phase origin defined as the frequency where the electrical length is zero is not known. Therefore the phase offset, denoted as ξ in 3.31, is unknown. This is not of a concern to us since we are only interested in relative measurements and changes in β.

The next objective is to find the characteristic impedance of the CPW or Z_o. Since the 2-port network is terminated with a matched load, the reflection coefficient Γ and S_{11} are equivalent, therefore Z_o can be found from the straightforward reflection coefficient equation.

$$\Gamma = \frac{Z_L - Z_o}{Z_L + Z_o} \tag{3.33}$$

We now have enough data to extract the circuit parameters of interest from the measurement data. The complex propagation constant of a transmission line can be stated by the two forms below.

$$\gamma = \sqrt{(R + j\omega L)(G + j\omega C)} \tag{3.34}$$

$$\gamma = \alpha + j\beta \tag{3.35}$$

Also the characteristic impedance of a transmission line can be stated as a function of circuit parameters such that

$$Z_o = \sqrt{\frac{R + j\omega L}{G + j\omega C}} \tag{3.36}$$

Since we have presented the formulations to extract α, β and Z_o from the measurement data, we can substitute these values into 3.34 and 3.36 and extract the circuit parameters. Figs 3.14-3.18 illustrate the measured Z_o, β, α, L, and C, with overlays of the theoretical values calculated from the formulations presented in section 3.2.1 respectively.

The effective dielectric constant of the CPW is also extracted from the measurements using the following formulations

$$n = \frac{c_o \beta}{\omega} \tag{3.37}$$

$$\varepsilon = n^2 \tag{3.38}$$

where n is the refractive index, and ε is the dielectric constant. For a non-magnetic media 3.38 is valid. The measurement versus theoretical plot for the dielectric constant is shown in Fig. 3.19.

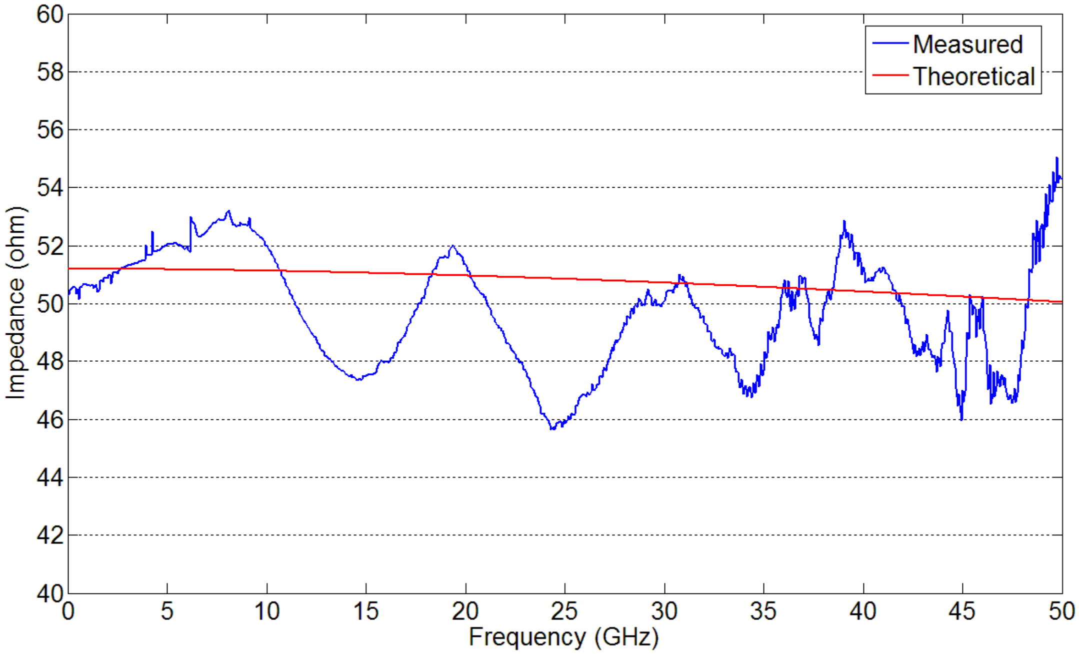

Figure 3.14 Theoretical and measured characteristic impedance Z_o for a YBCO CPW TL

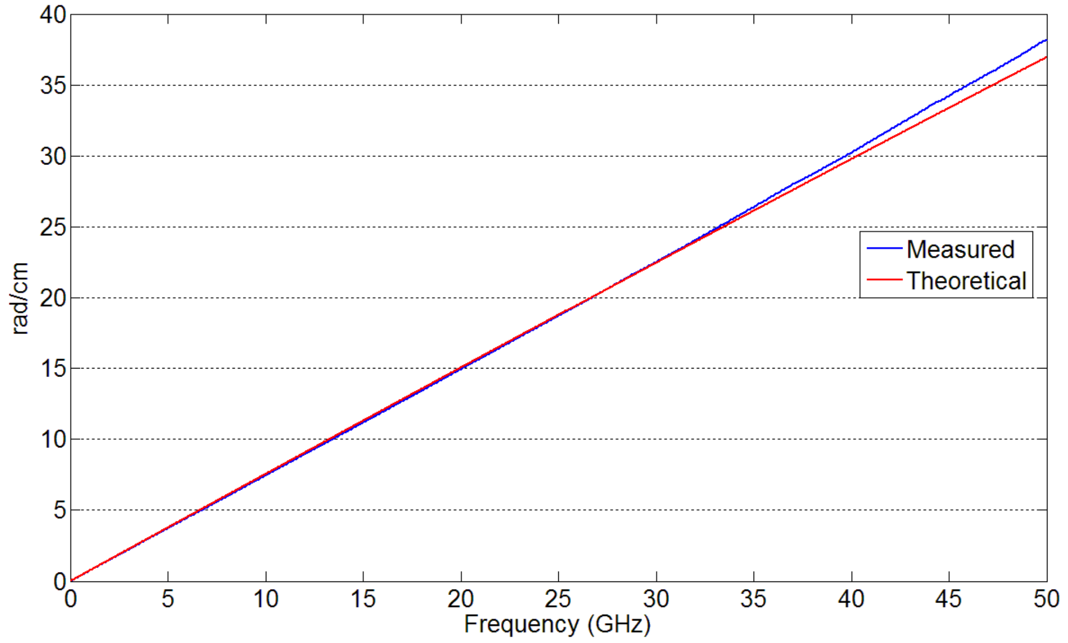

Figure 3.15 Theoretical and measured phase constant β for a YBCO CPW TL

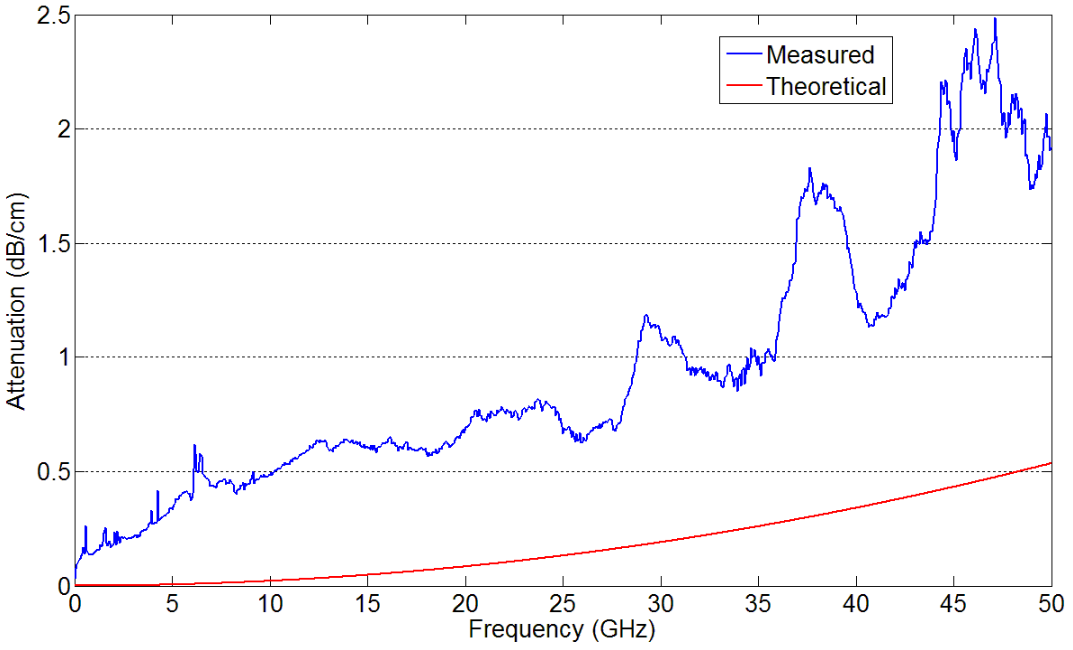

Figure 3.16 Theoretical and measured attenuation constant α for a YBCO CPW TL

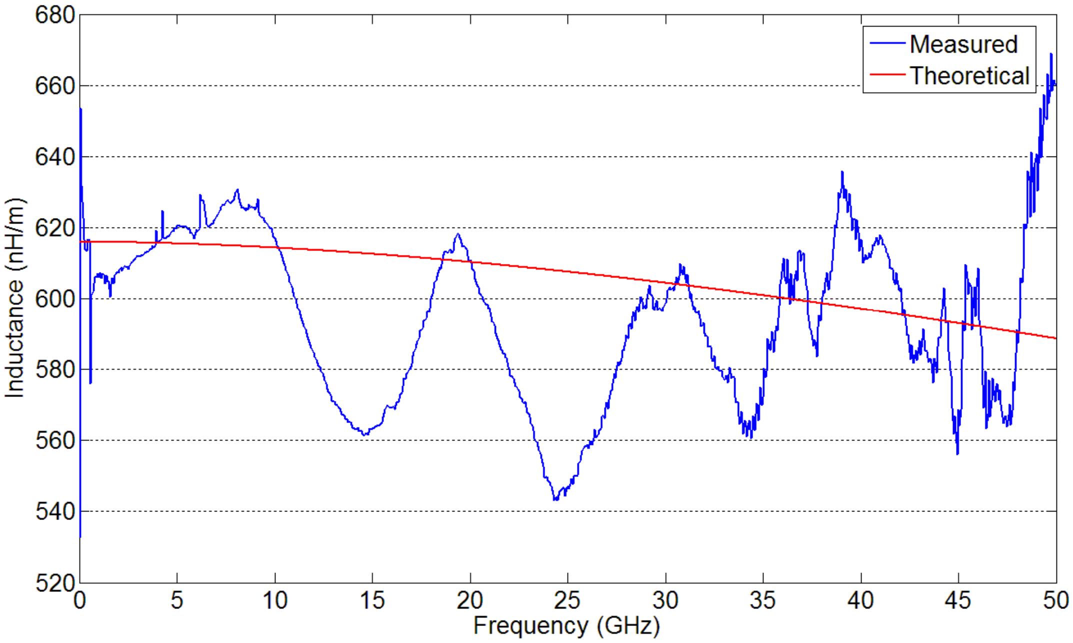

Figure 3.17 Theoretical and measured inductance per meter for a YBCO CPW TL

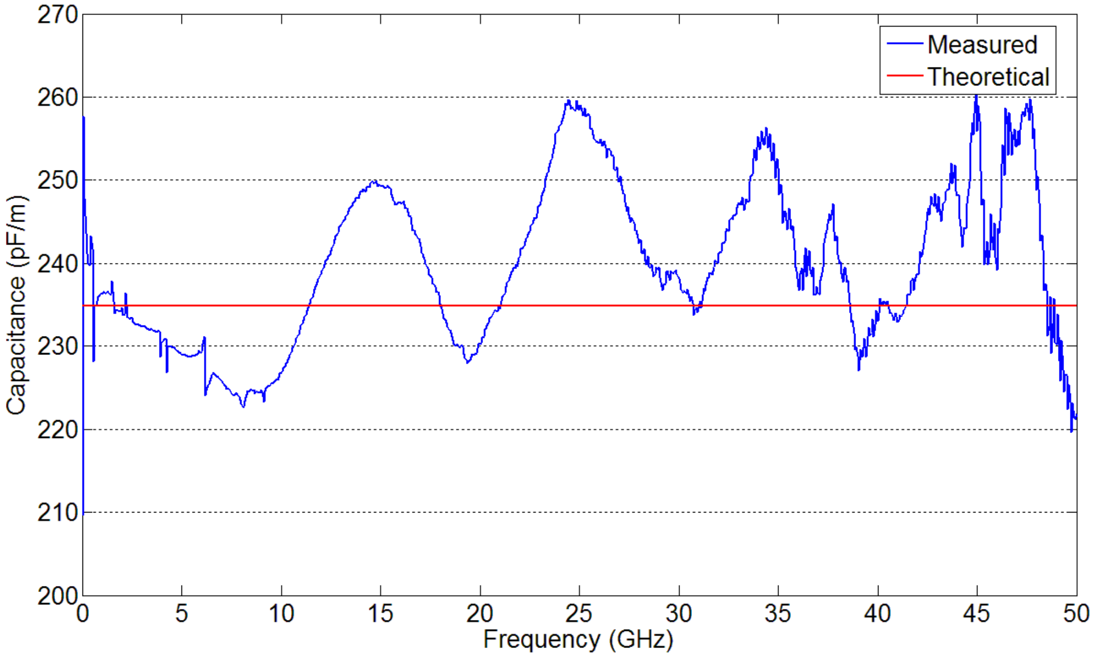

Figure 3.18 Theoretical and measured capacitance per meter for a YBCO CPW TL

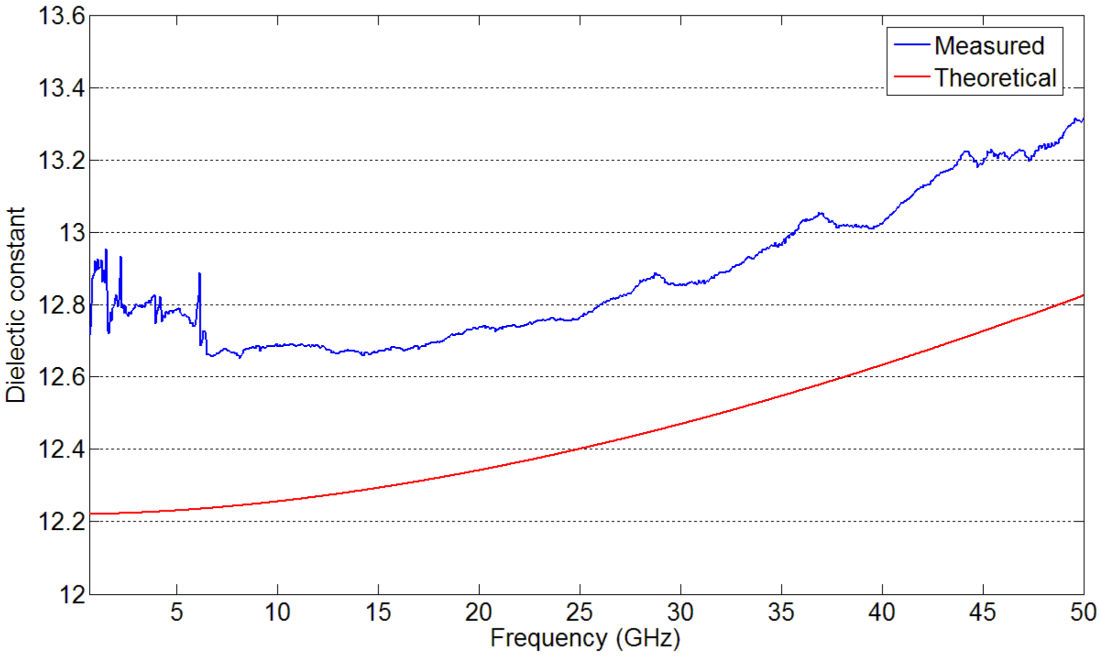

Figure 3.19 Theoretical and measured dielectric constant for a YBCO CPW TL

It is evident from the plots in Fig. 3.14-3.19 that there is a good correlation between the theoretical calculations and the measurement data. Referring to Z_o, L and C, there are several oscillations in the measured data around the theoretical value. This can be attributed to the resonances that are observed in the actual S-parameters as seen in Fig. 3.10 and Fig. 3.11. Due to the physical length of the TL, at certain frequencies the electrical length of the TL is several wavelengths long. This creates small resonances in the structure, creating these oscillating discrepancies. It should be noted that this disparity is quite small and does not have a great effect of the device performance.

The attenuation of the CPW is also larger then what the theory predicts. The theory predicts an insertion loss of 0.5dB/cm at 50GHz, however the measured data is closer to 2dB/cm. This can be attributed to the two extra contact resistances created between the probes and the gold pads and the gold and the YBCO film, which are not accounted for in the theoretical calculations.

We have introduced a methodology to design superconducting transmission lines, and used it to fabricate a YBCO CPW with exceptional performance. In the following section, this CPW design will be adopted as the framework for the microwave photonic devices.

Chapter 4

Microwave Photonics in YBCO Thin Film Devices

The typical material used for microwave photonic functions are semiconductors, since all the components of such a system, namely lasers, waveguides, detectors, can be fabricated by semiconductors with easy integration. However, the increasing demand for future communications system drives the research to achieve higher speeds, ultra-low noise characteristics, and low power consumption. Superconducting optoelectronics are one of the most competitive technologies in the realization of these needs.

The study of superconductors when perturbed by external stimulations such as optical illumination is an interesting phenomena for understanding the basis behind Cooper pair breaking mechanisms and for using this effect for practical applications [47]-[56]. The changes created in the superconductor when optically illuminated results from changes in the superconducting carrier density. Two mechanisms can be identified to describe the optical mechanism in a superconductor, a bolometric and non-bolometric photoresponse. A bolometric response is a thermal response caused by local heating of the superconducting film. Typically it is associated with a change in the resistance of the film. The non-bolometric response is due to the modulation of the Cooper-pairs density or the kinetic inductance associated with superconductors, by optical excitation. The main criteria to distinguish between a bolometric and non-bolometric response is the speed of the response. Photoresponse events generated from superconductors tend to have fast and slow components. Fast components are assumed to be non-bolometric, whereas slow components due to thermal heating are generally considered to be bolometric. However, it has been shown that fast bolometric response times of sub nanoseconds are also realizable from high T_c thin films [57]. In either case, the density of Cooper pairs in a superconductor can be varied by optical radiation, in turn changing the associated kinetic inductance.

This section presents the laser irradiated frequency domain measurement techniques and results, investigating the optical response of a YBCO microwave resonator and delay line. Whatever the physics responsible for the observed behavior from the YBCO film, it is interesting to study the effect of light on the microwave properties to implement and design useful and practical devices.

4.1 YBCO Meander Lines

The device used to realize the microwave photonic process is a meander line structure. It was fabricated by the method described in section 3.1. The meander line is placed in the center of the CPW structure introduced in section 3.2, with appropriate tapers connecting the 60μm wide center strip to the meander line. Two different structures are designed. The first meander line consists of a 3μm line width and 3μm wide spacing between each turn. The overall area of the meander structure covers 176μm x 201μm. This device will be referred to as the 3μm meander. The second meander line consists of a 5μm line width and 5μm wide spacing between each turn. The overall area of the meander structure covers 176μm x 195μm. This device will be referred to as the 5μm meander. Images of both devices are shown in Fig. 4.1. The devices were measured in the probe station described in section 2. S-parameters for both the 3μm meander and 5μm meander measured with an RF power of -17dBm, are shown in Fig. 4.2 and Fig. 4.3 respectively.

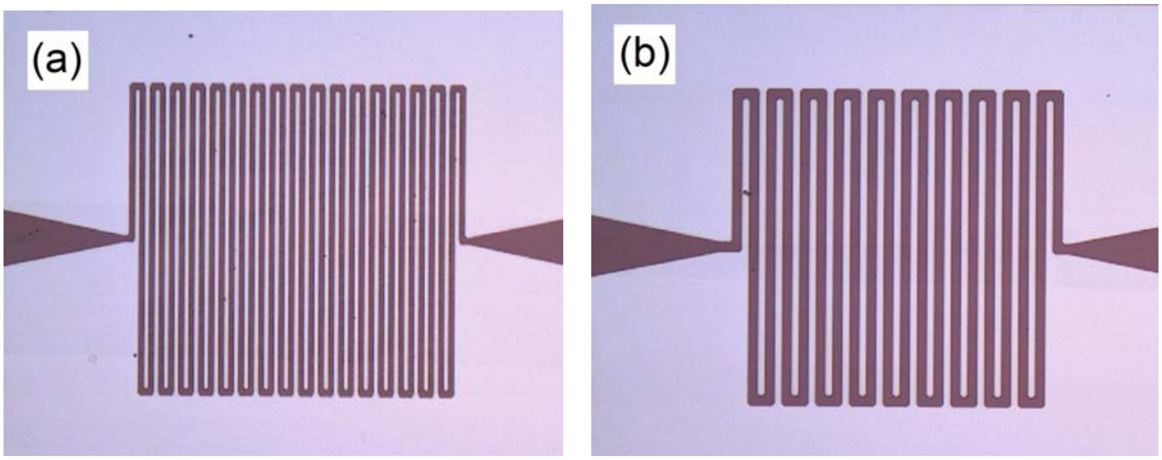

Figure 4.1 (a) 3μm line width and spacing meander line & (b) 5μm line width and spacing meander line

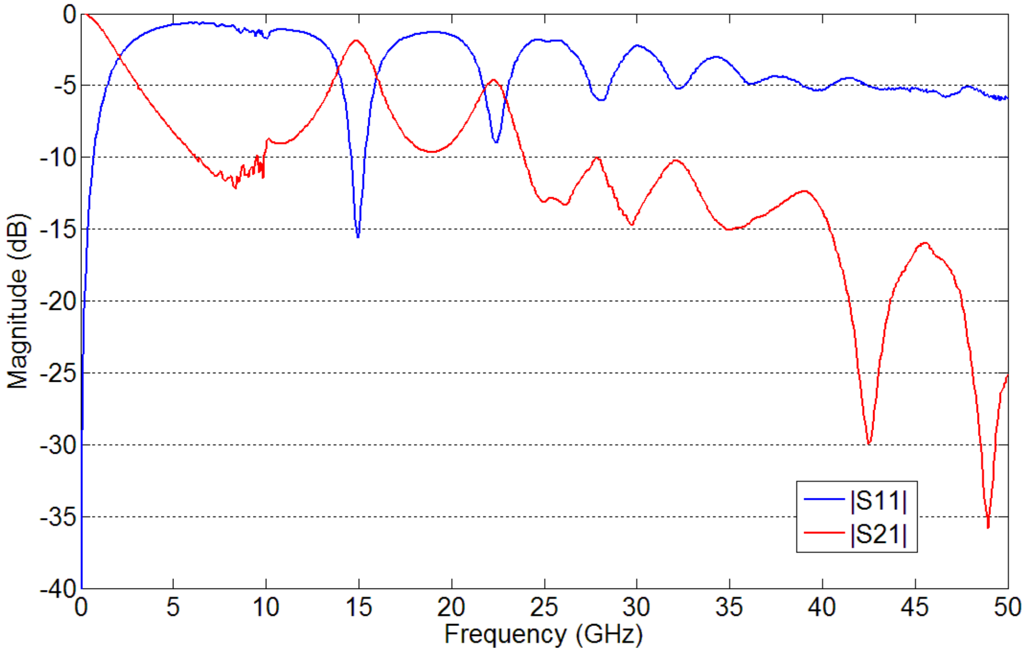

Figure 4.2 Magnitude of S_{11} and S_{12} for 3μm meander line

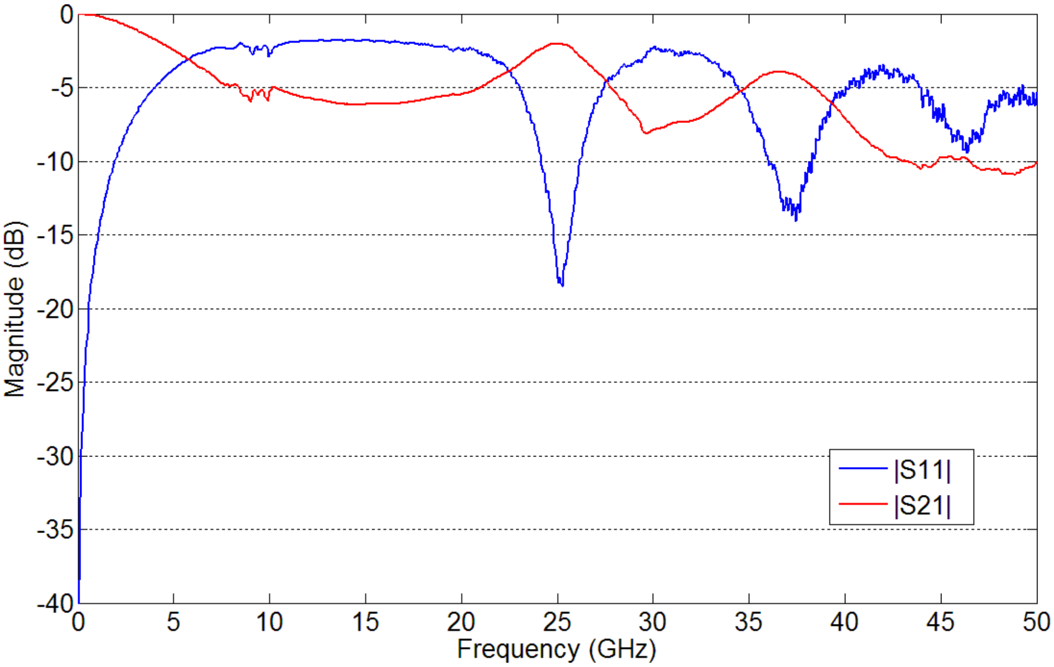

Figure 4.3 Magnitude of S_{11} and S_{12} for 5μm meander line

From Fig.4.2 we can see clear resonances at 15GHz, and 22.5GHz for the 3µm meander. We will concentrate on the first resonant peak. The insertion loss is 2dB, and the return loss is about 16dB. From Fig.4.3 we can observe two resonances at 25GHz and 37.5GHz for the 5µm meander. Again we will move our attention to the first resonance. The insertion loss is 2dB with a return loss of 19dB. The strategy is to couple a laser to the meander line and observe the changes in the microwave performance. These results are presented in the following sections.

4.2 Optically Tunable YBCO Microwave Resonator

A block diagram of the measurement setup is shown in Fig. 4.4. The microwave measurement is performed using the same procedure described in the previous section. The Agilent 8364B network analyzer is used to obtain the 2-port S-parameters. The fiber optic probe arm described in section 2.3 is used to excite the meanders with light. A 1550nm continuous wave (CW) laser diode source is used to illuminate the superconducting meander line. The laser diode is fed into a variable attenuator, followed by an Erbium Doped Fiber Amplifier (EDFA) from Oclara™, model PG300.

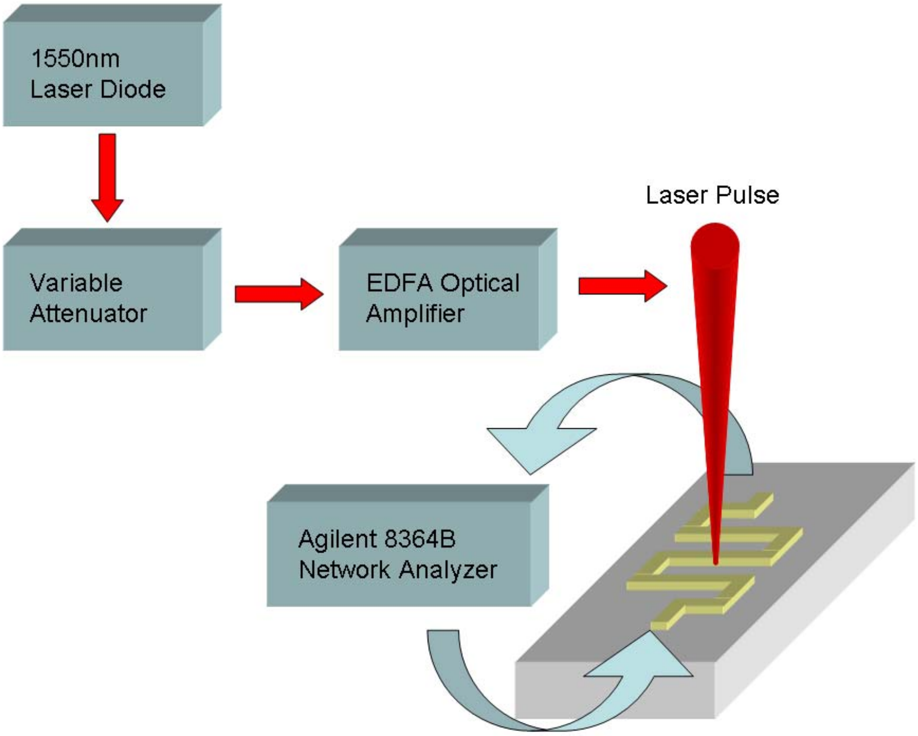

Figure 4.4 Block diagram for optically tunable YBCO microwave resonator measurement

Using the optical setup proposed, the incident optical power can be controlled between 0 to 15dBm (0 – 32mW), as measured with a commercial power meter. The spot size can be adjusted by controlling the vertical position of the optical fiber probe tip with respect to the wafer surface. A red laser is used for alignment to ensure the beam spot uniformly covers the entire area of the meander line uniformly.

4.2.1 3µm Meander Line as a Tunable Resonator

Fig 4.5 shows the magnitude of S_{21}, illustrating the shift in resonance for the 3µm meander line with varying optical power. Fig. 4.6 shows the corresponding S_{11} plot under the same conditions. The frequency range of interest is limited to 10GHz-18GHz, concentrating on the first and most prominent resonant peak. The shifts in the resonance peak go from right to left with increasing optical power from the 1550nm CW laser.

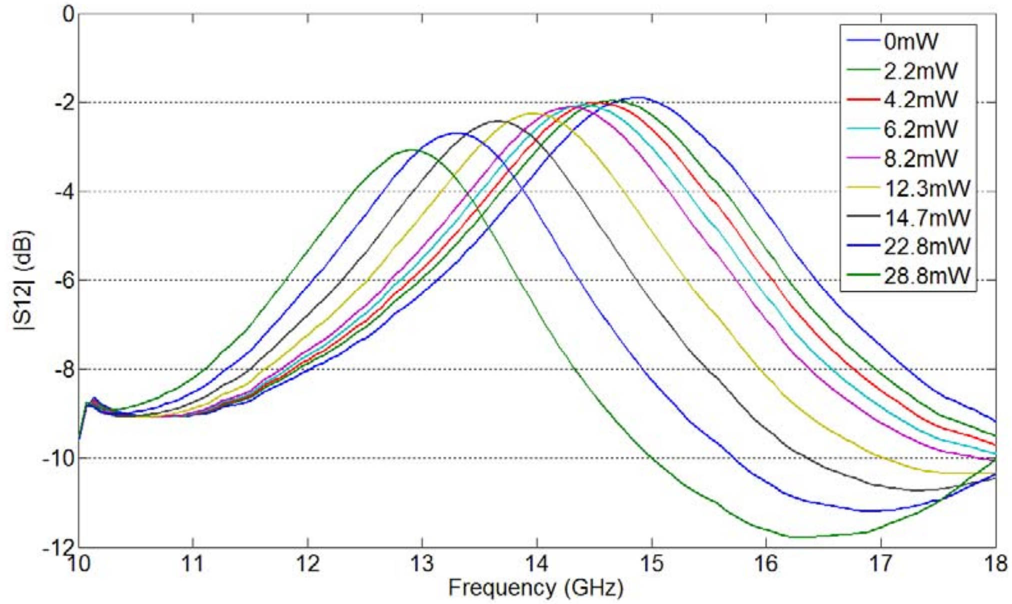

Figure 4.5 Magnitude of S_{21} for the 3µm meander line under optical excitation

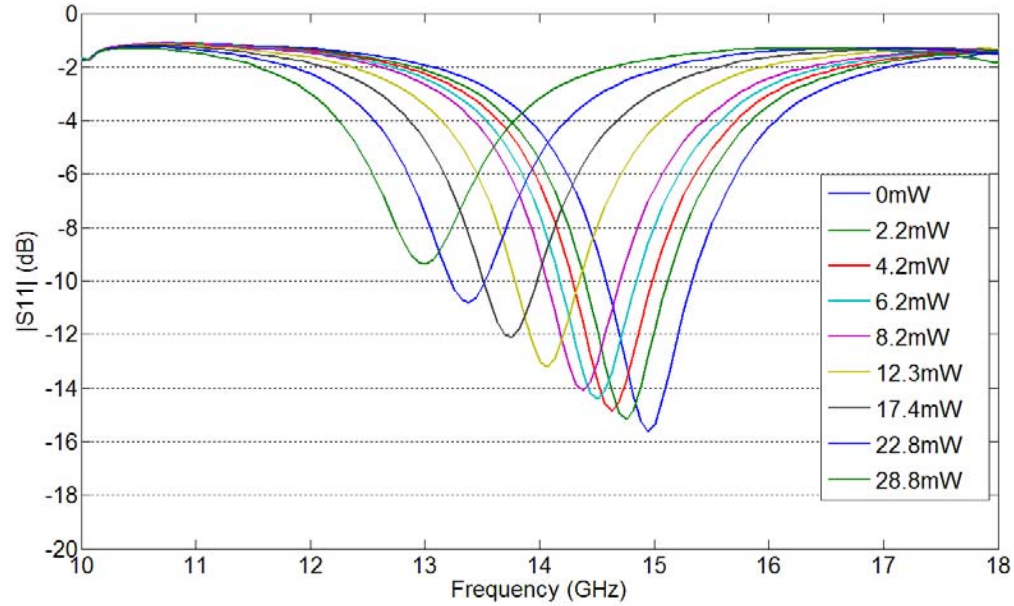

Figure 4.6 Magnitude of S_{11} for the 3μm meander line under optical excitation

With no illumination, the resonant frequency of the meander line is 15GHz with an insertion loss of 2dB. As the optical power is increased, the resonant peak shifts downward due to the breaking of Cooper-pairs by optical excitation. This in turn increases the kinetic inductance of the superconductor, shifting the resonance of the device. At the maximum output optical power of 28.8mW the resonant peak shifts to 12.9GHz. A shift of 2.1GHz has been achieved. Two different regions of operation have been observed during this experiment. The first region is a shift in the resonant frequency with a minimal effect on attenuation. Up to 8.2mW of optical power, the attenuation at the peak increases by only 0.2dB. The second region is a change in the resonant frequency, along with an increase in the attenuation. At the full optical output power of 28.8mW the insertion loss at the resonant peak is 3dB. Therefore, the shift in resonant frequency is accompanied by an increase in the attenuation at the resonant peak. A plot illustrating the change in resonance for varying optical power is shown in Fig. 4.7.

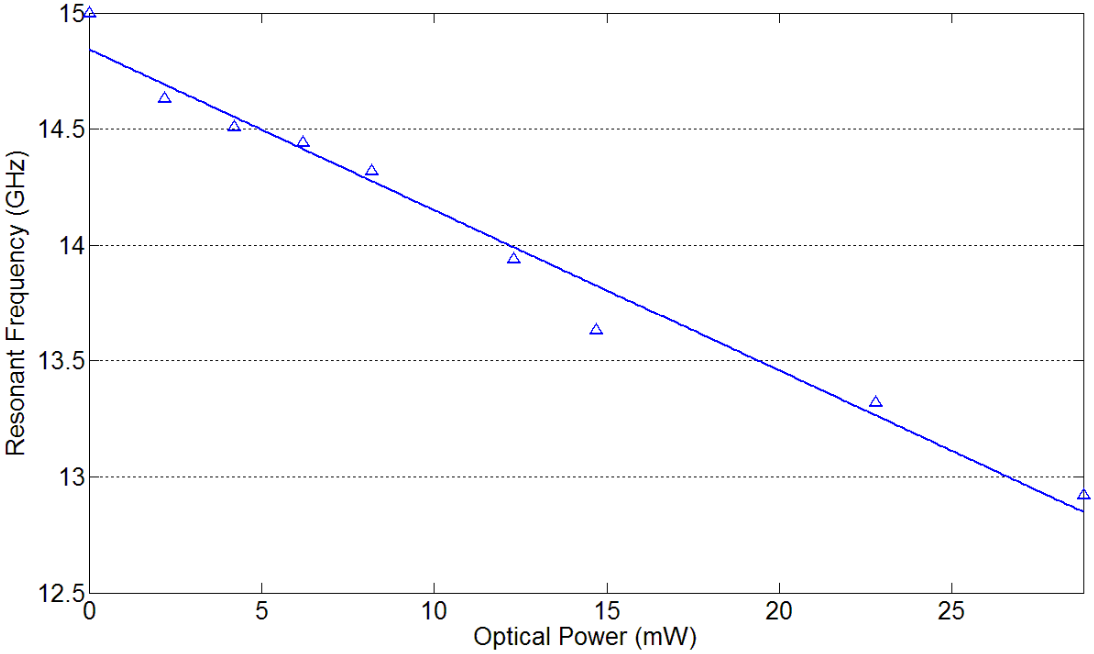

Figure 4.7 Resonant frequency vs. input optical power for 3µm meander line

4.2.2 5µm Meander Line as a Tunable Resonator

Fig 4.8 shows the magnitude of S_{21}, illustrating the shift in resonance for the 5µm meander line with varying optical power. Fig. 4.9 shows the corresponding S_{11} plot under the same conditions. The frequency range of interest is limited to 16GHz-32GHz, concentrating on the first and most prominent resonant peak. The shifts in the resonance peak go from right to left with increasing optical power from the 1550nm CW laser.

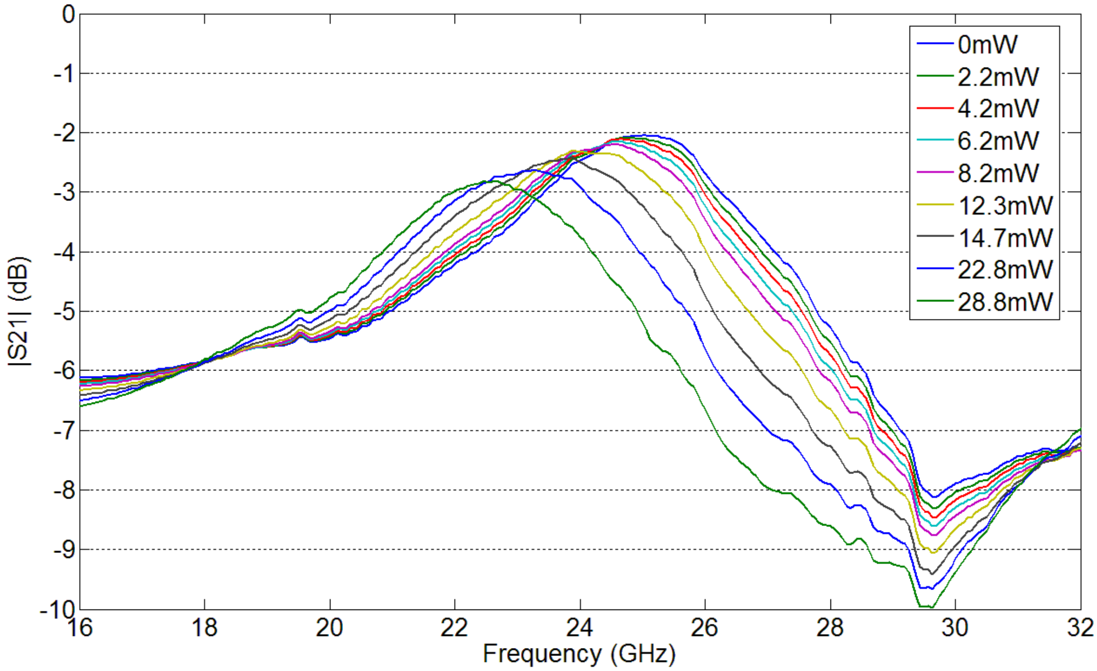

Figure 4.8 Magnitude of S_{21} for the 5μm meander line under optical excitation

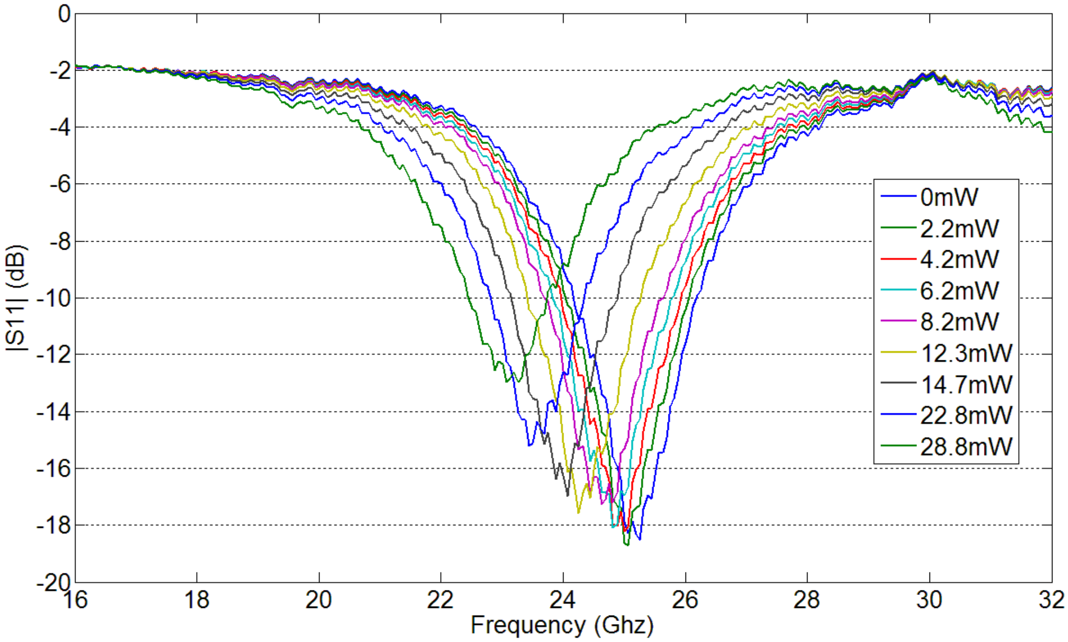

Figure 4.9 Magnitude of S_{11} for the 5μm meander line under optical excitation

With no illumination the resonant frequency of the 5µm meander line is 25GHz with an insertion loss of 2dB. As the optical power is increased, the resonant peak shifts down in frequency, similar to what was observed for the 3µm meander line. At the maximum output optical power of 28.8mW the resonant peak shifts to 22.5GHz. A shift off 2.5GHz has been achieved. Similar to the 3µm meander device, two different regions of operation have been observed during this experiment. The first region is a shift in the resonant frequency with a minimal effect on attenuation. Up to 8.2mW of optical power, the attenuation at the peak increases by only 0.2dB. The second region provides a shift in the resonant frequency, along with an increase in attenuation. With the full optical output power of 28.8mW the insertion loss at the resonant peak is 2.8dB. Therefore, the resonance shift is accompanied by an increase in attenuation. A plot illustrating the change in resonance for varying optical power is shown in Fig. 4.10.

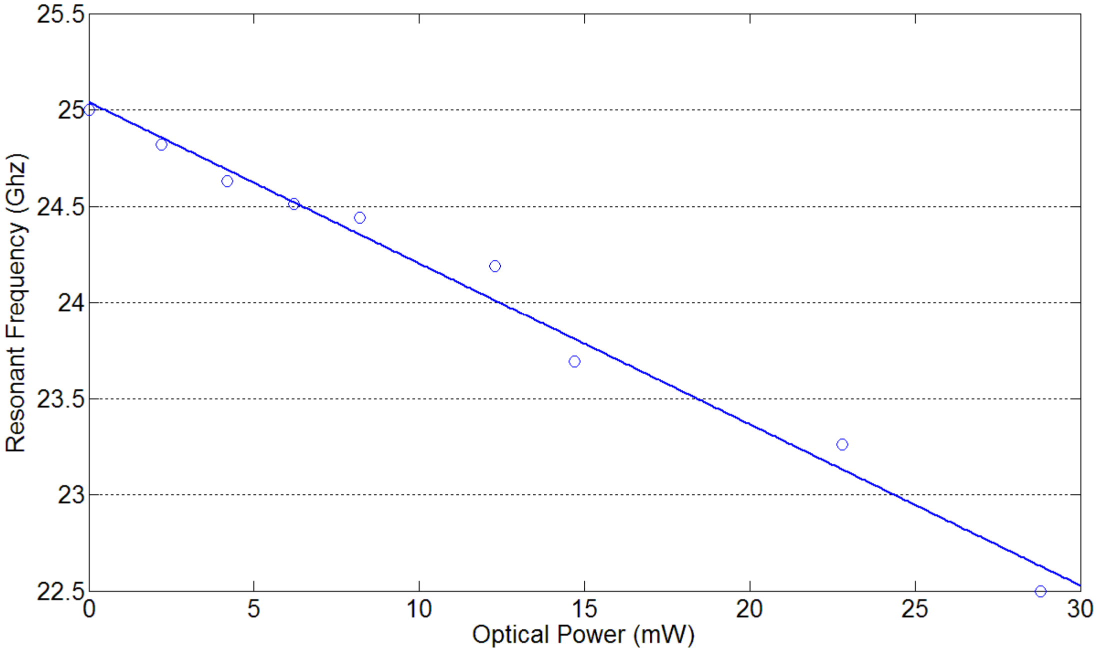

Figure 4.10 Resonant frequency vs. input optical power for 5µm meander line

4.3 Optically Tunable YBCO Delay Line

The meander lines presented in the previous section will now be utilized to realize a tunable microwave delay line. The same arguments used to justify a tunable resonator with incident optical power on a superconductor can be adopted. By modulating the superconducting carrier density and consequently the kinetic inductance, a change in the phase of a microwave signal can be realized. The measurement setup is the same as that shown in Fig. 4.4. Each meander line will be irradiated with optical power and the effect of the delay will be characterized for each device.

4.3.1 3μm Meander Line as a Tunable Delay Line

Fig 4.11 shows the phase of S_{21}, illustrating the shift in the phase delay for the 3μm meander line with varying optical power.

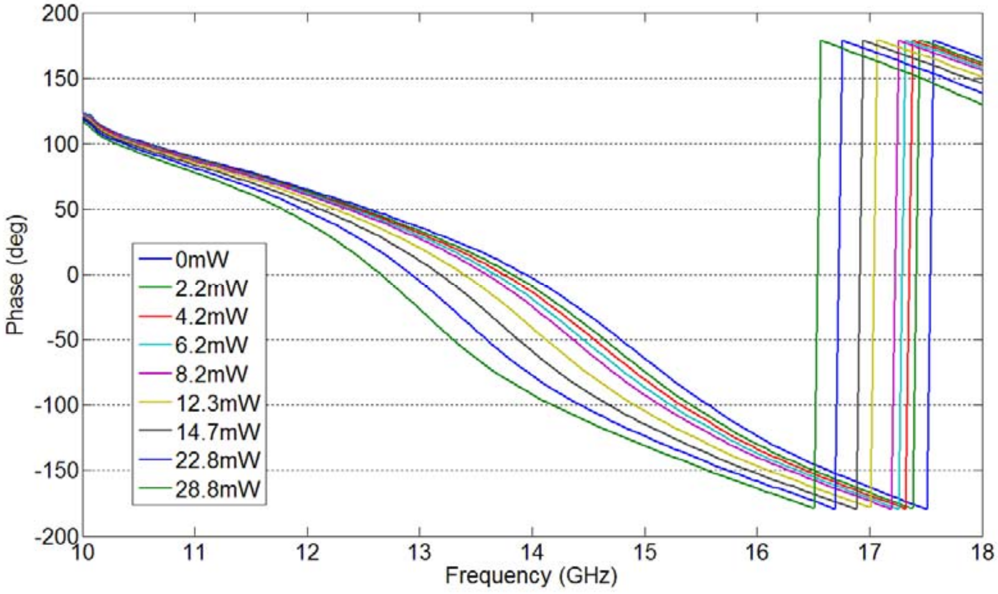

Figure 4.11 Phase shift vs. input optical power for 3μm meander line

We move our attention to 14GHz, which is observed to be the ideal operating point for this device as a tunable delay line. The phase shift at 14GHz upon illumination of the meander line is fairly linear, as shown in Fig. 4.12. At maximum optical intensity of 28.8mW the phase shift is 92.3 degrees. With no optical illumination the insertion loss at 14GHz is 3.5dB. At maximum optical intensity the 92.3 degree phase shift is accompanied by an insertion loss of 6.1dB, an increase of approximately 2.6dB in attenuation. The insertion loss at different frequencies can be seen from the $|S_{21}|$ plot in Fig. 4.5. For the purpose of a phase shifter at 14GHz, the attenuation with varying optical power is shown in Fig. 4.13. The shape of the attenuation vs. optical power curve is strongly dependent on the frequency of operation selected for the delay line, resulting from the shape of the magnitude response of S_{21}.

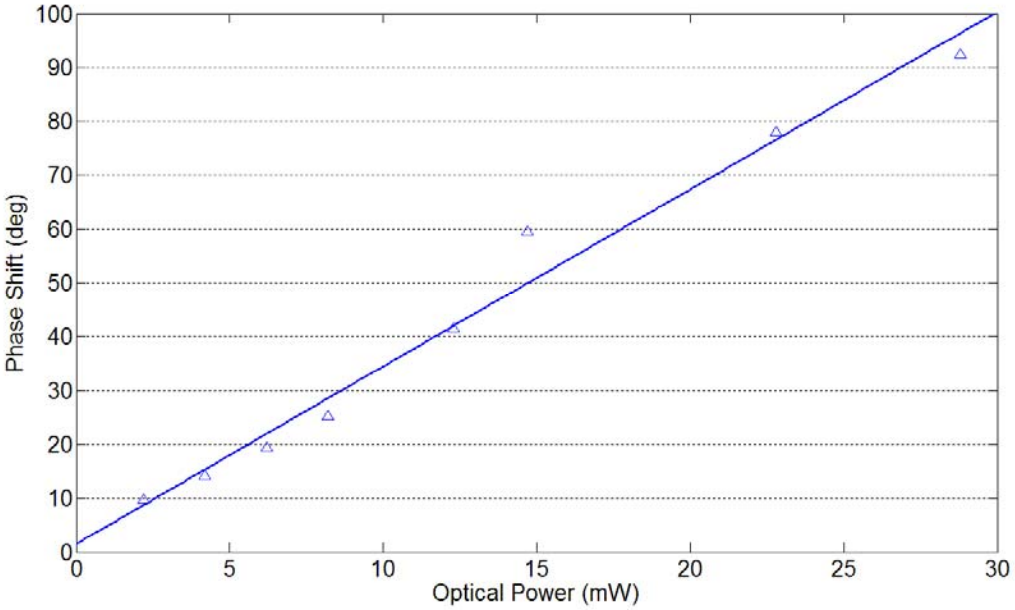

Figure 4.12 Phase shift @ 14GHz vs. input optical power for 3μm meander line

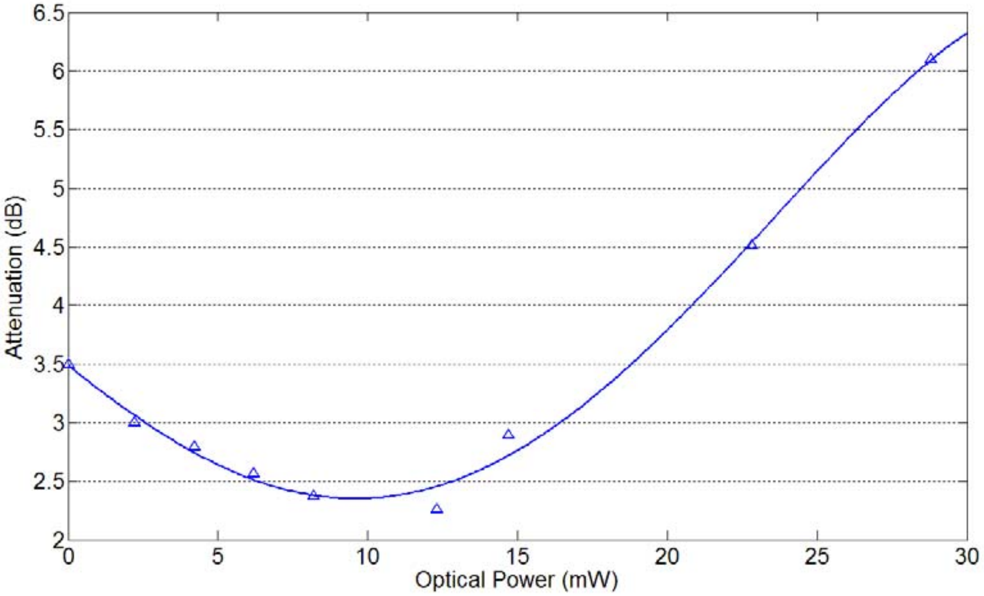

Figure 4.13 Attenuation @ 14GHz vs. input optical power for 3μm meander line

4.3.2 5µm Meander Line as a Tunable Delay Line

Fig. 4.14 shows the phase of S_{21}, illustrating the shift in the phase delay for the 5µm meander line with varying optical power.

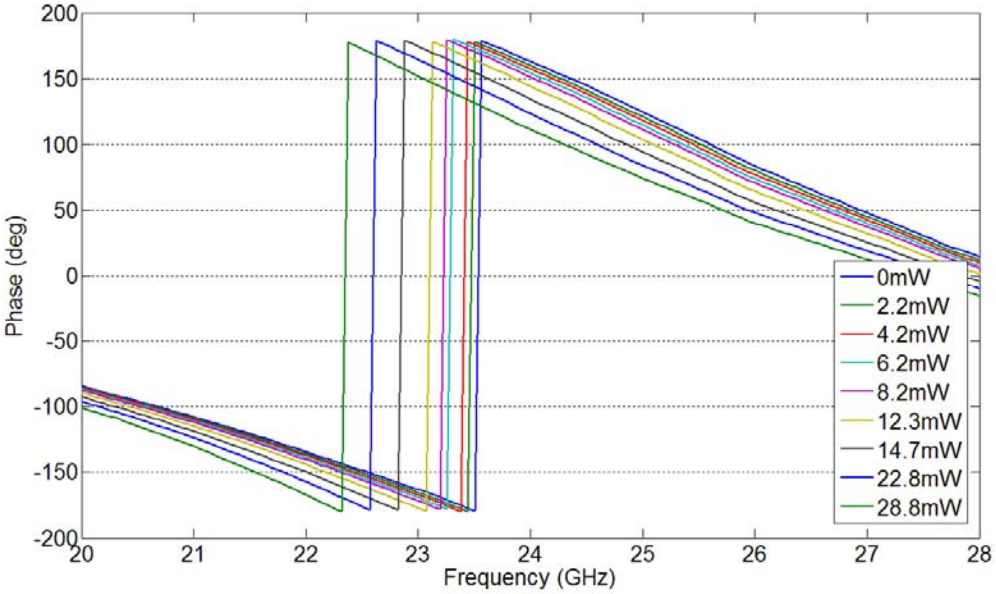

Figure 4.14 Phase shift vs. input optical power for 5µm meander line

We move our attention to 24GHz, which is observed to be the ideal operating point for this device as a tunable delay line. The phase shift at 24GHz upon illumination of the meander line is fairly linear, as shown in Fig. 4.15. At maximum optical intensity of 28.8mW the phase shift is 52 degrees. With no optical illumination the insertion loss at 24GHz is 2.5dB. At maximum optical intensity the 52 degree phase shift is accompanied by an insertion loss of 3.7dB, an increase of approximately 1.2dB in attenuation. The insertion loss at different frequencies can be seen from the $|S_{21}|$ plot in Fig. 4.8. For the purpose of a phase shifter at 24GHz, the attenuation with varying optical power is shown in Fig. 4.16. The shape of the attenuation vs. optical power curve is strongly dependent on the frequency of operation selected for the delay line, resulting from the shape of the magnitude response of S_{21}.

From the measurements we can conclude that the 3µm meander line provides a greater phase shift of 92.3 degrees compared to the 52 degrees phase shift of the 5µm meander, at a cost of higher attenuation. At maximum optical irradiation, the 3µm meander line exhibits an insertion loss of 6.1dB compared to the 5µm meander line with an insertion loss of 3.7dB.

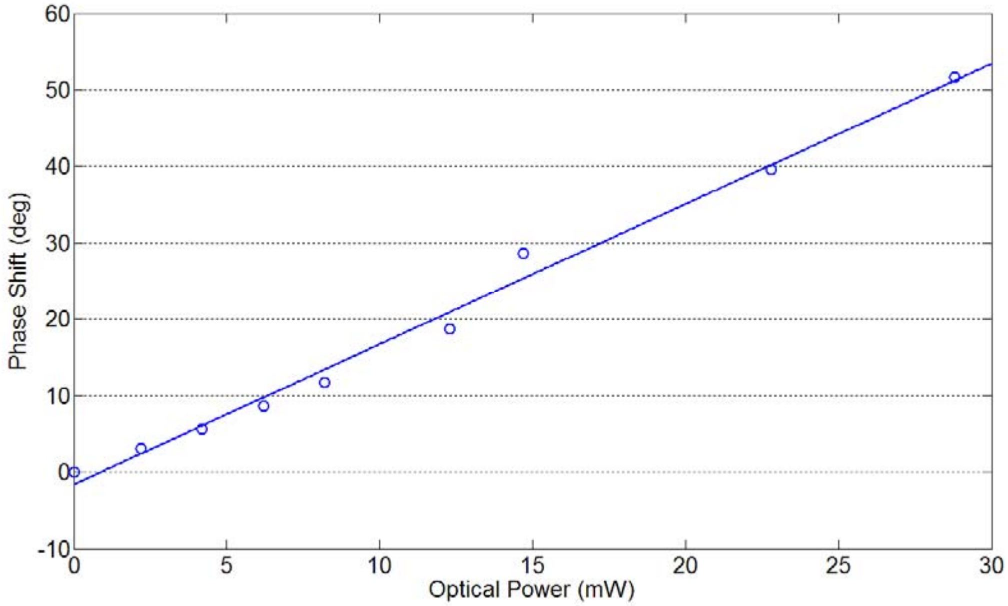

Figure 4.15 Phase shift @ 24GHz vs. input optical power for 5μm meander line

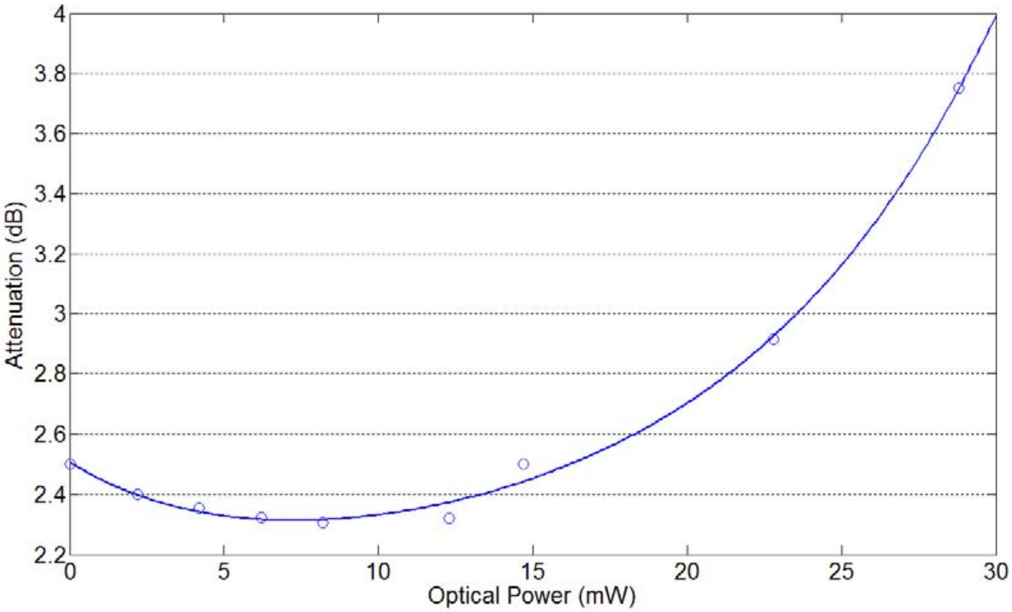

Figure 4.16 Attenuation @ 24GHz vs. input optical power for 5μm meander line

Chapter 5

Picosecond Photoresponse Measurements

The study of the fast photoresponse of superconducting thin films has been extensively investigated due to its interesting physics and its practical applications in novel devices [58]-[66]. As discussed in the Chapter 4, two mechanisms exist describing the optical mechanism in superconductors, bolometric and non-bolometric photoresponse. To reiterate the point, a bolometric response is a response created by the incident radiation being converted into heat, thereby changing the resistance of the superconductor. A non-bolometric response is a response due to the modulation of the super current carrier density, the Cooper pairs, thereby modulating the kinetic inductance of the superconductor. The fast photoresponse in superconductors is typically attributed to this type of mechanism. In a current biased superconducting device, a change in the kinetic inductance by optical excitation will produce a voltage across the device. This voltage constitutes the photoresponse.

In this experiment, the 3μm meander line introduced in Chapter 4 for the purpose of microwave photonic characterization will be used as a picosecond photodetector. Two different regimes of operation will be shown, one with a fast photoresponse in the picosecond range and another with a slow photoresponse in the nanosecond range. A current source will supply a bias current to the device, and an optical fiber will couple a pulsed laser to the meander line in a similar fashion to what was described in Chapter 4. The photoresponse is measured on a high-speed oscilloscope with a 16GHz bandwidth. A microwave amplifier is used to amplify the photoresponse from the superconducting meander line and is then measured with an oscilloscope. The pulsed laser used in this experiment is the Id Quantique 1550nm short pulse laser source, model number id-300-1550. The pulse is amplified by an EDFA, providing a full width half maximum (FWHM) pulse duration of 45ps with an average power that can be controlled by the EDFA. The microwave amplifier used in this experiment is the Philips Scientific 6954. It has a gain of 100 and a bandwidth cutoff at 1.8 GHz. Therefore, the response of the photodetector will be limited by the bandwidth of the amplifier. A block diagram of the experiment setup is shown in Fig. 5.1. The current source is provided by a battery to ensure a stable current bias.

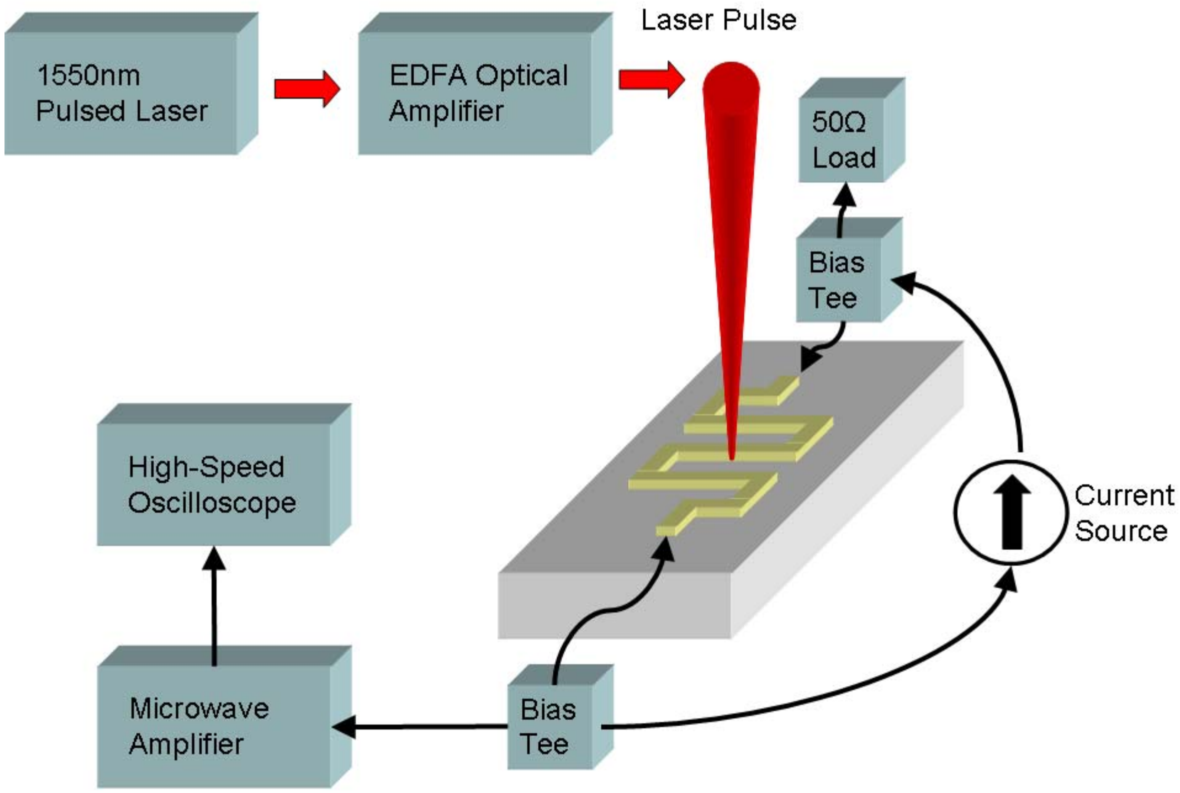

Figure 5.1 Block diagram of the photodetection experiment

The current-voltage (I-V) curve of the 3μm meander line has been measured to determine the critical current of the device. This value is used to current bias the device at the appropriate bias point to measure the photoresponse. The I-V curve of the 3μm meander line is shown in Fig. 5.2. The voltage begins to move off the zero voltage axis at 5.5mA which we will define as the critical current of the device. The bias current dependence of the photoresponse is examined for the 3μm meander line. Fig. 5.3 illustrates the photoresponse of the meander line to a 45ps laser pulse with an average power of 3.5mW using a repetition rate of 1MHz. The bias current is varied from 5mA to 6.5mA.

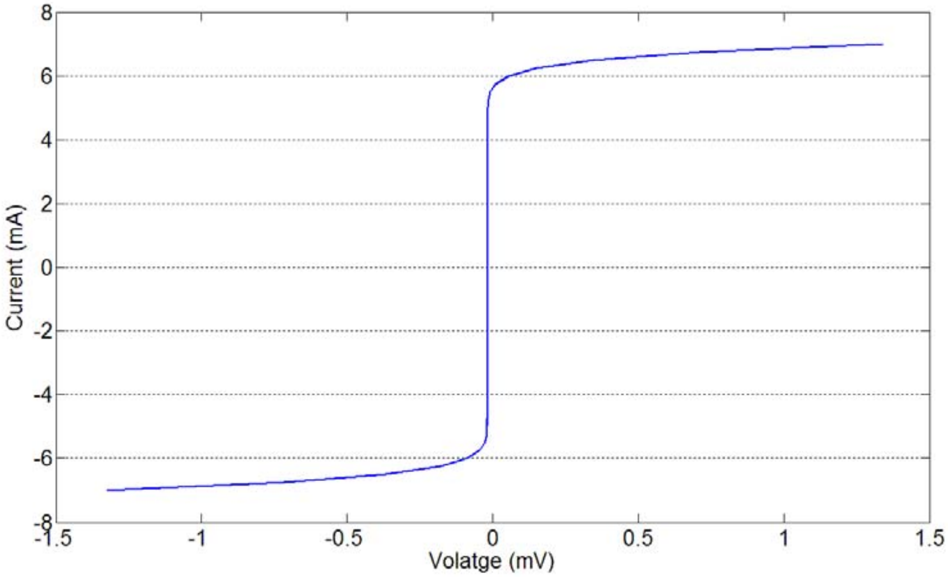

Figure 5.2 Current-voltage characteristic for 3µm meander line.

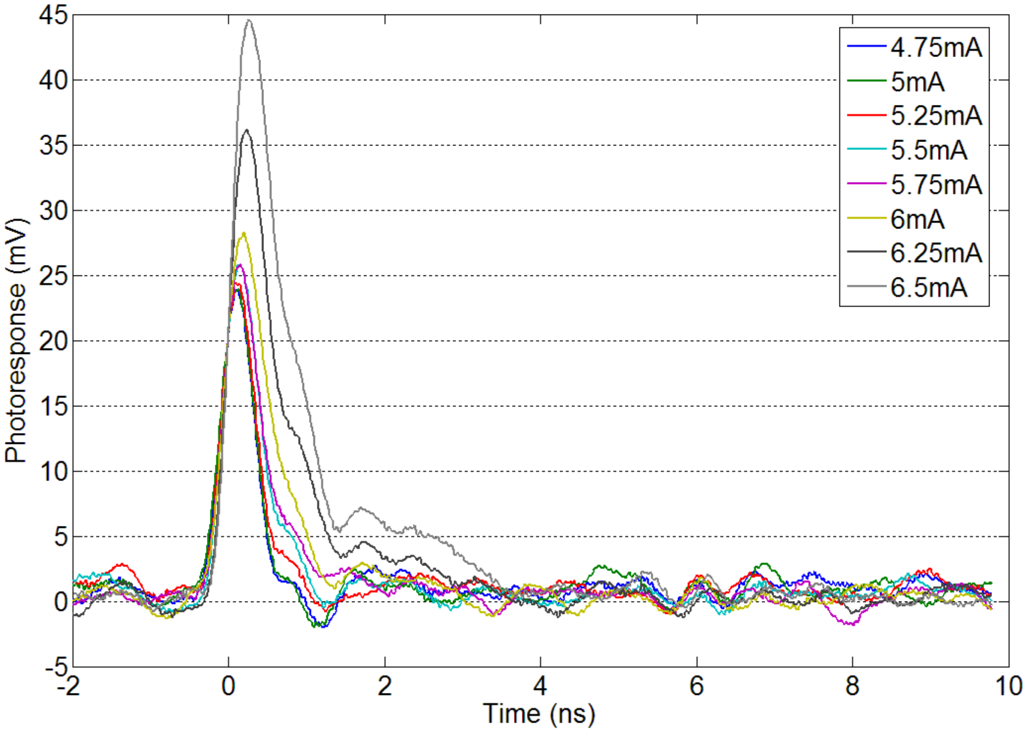

Figure 5.3 Bias current dependence on the photoresponse for the 3µm meander line

A fast photoresponse is observed for bias currents below 5.5mA, with a rise time of 280ps and a FWHM photoresponse pulse duration of 500ps. There is a sudden increase in the amplitude of the photoresponse past 5.5mA, which coincides with the critical current of the device. This increase corresponds to the resistive transition region of the device accompanied by a slower photoresponse mechanism. At 6.5mA the rise time of the photoresponse remains similar to the low bias current case however the recovery time for the detection event is much greater. The FWHM pulse duration increases to approximately 770ps, but the complete recovery back to the zero voltage state elapses approximately 3.5ns. This is very characteristic of a bolometric photodetector; the time required for the heat to dissipate into the heat sink is generally a slow process. The speed of the detector is depended on the thermal time constant to remove the heat from the superconductor.

Fig. 5.4 illustrates the bias current dependence on the peak amplitude of the photoresponse. The figure shows the linear increase with the amplitude at small bias currents where only a fast photoresponse was observed. There is an abrupt increase in the amplitude of the photoresponse past 5.5mA due to the superconductor entering the resistive region. This region is also accompanied by a slower photoresponse.

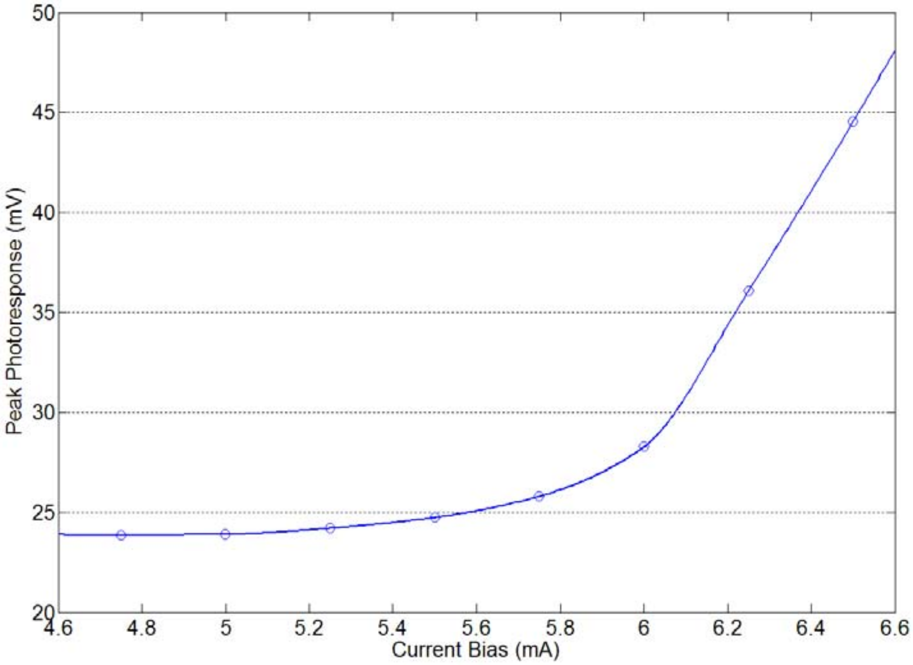

Figure 5.4 Bias current dependence on the peak photoresponse for the 3μm meander line

Next, the optical power dependence of the photoresponse is examined for the 3μm meander line. Fig. 5.5 illustrates the photoresponse of the meander line biased at a constant current of 5.5mA, to a 45ps 1550nm laser pulse using a repetition rate of 1MHz. The average optical power of the laser is varied from 2.5mW to 4.9mW.

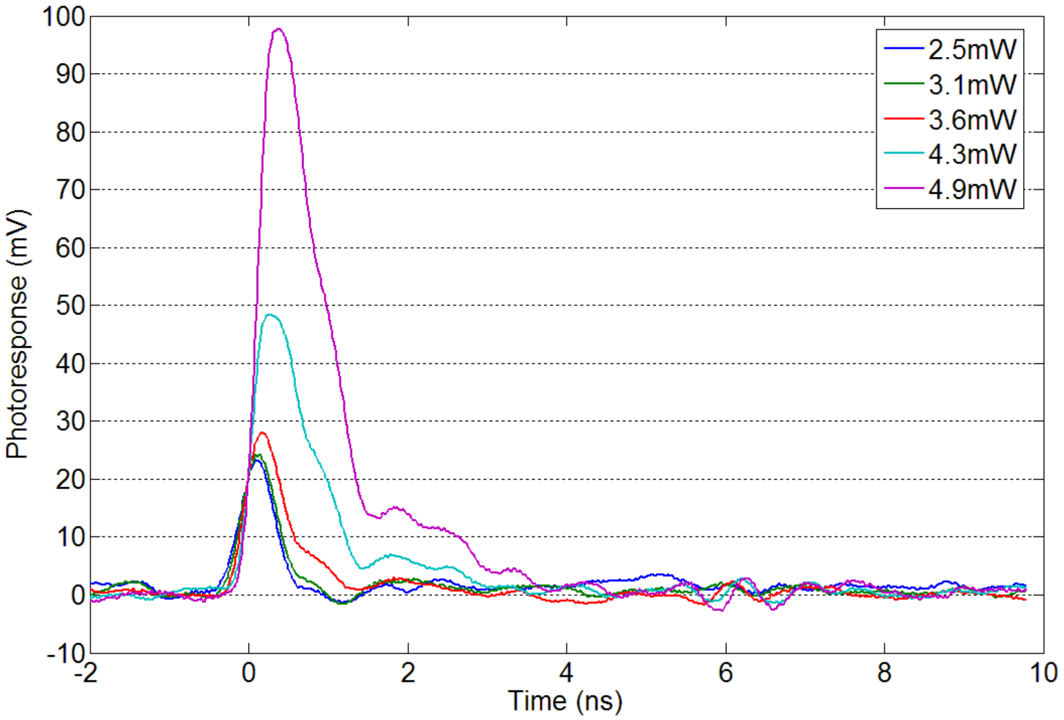

Figure 5.5 Optical power dependence on the photoresponse for the 3μm meander line biased at a constant current of 5.5mA

A fast photoresponse is observed for an average optical power between 2.5mW to 3.6mW, with a rise time of 280ps and a FWHM photoresponse pulse duration of 500ps. There is a sudden increase in the amplitude of the photoresponse past 3.6mW of average optical power. The photoresponse behavior is similar to the photoresponse of the meander line biased with a high current. The high optical power drives the film into the resistive region generating a slow photoresponse mechanism. At 4.9mW of average optical power the rise time remains relatively constant at 280ps, however the FWHM photoresponse pulse duration increase to about 880ps. The complete recovery back to the zero voltage state elapses approximately 3.5ns. This is characteristic of a bolometric photoresponse where the speed of detection is depended on the thermal time constant of the device.

Therefore, it has been shown that the 3μm meander line can operate as a picosecond photodetector, and the characteristics of the photoresponse depends greatly on the operating conditions. A fast photoresponse can be observed if the superconductor is not driven into the resistive regime, while a slower photoresponse is observed when the superconductor is locally heated and driven into the resistive transition. At this point it should be noted that the speed of the photodetector is limited by the bandwidth of the microwave amplifier. The 280ps rise time could very well be much faster however the 1.8GHz bandwidth of the microwave amplifier limits the speed of the measurement.

Chapter 6

I-V Measurements of Weak Link Junctions

Josephson junctions are an attractive area of research because of their potential use in many practical applications from quantum computing, to medical instrumentation, sensors, and electronic devices. They also provide enormous insight into the nature of superconductivity. There are several different configurations to realize Josephson junctions. Fig. 6.1 illustrates several of these topologies.

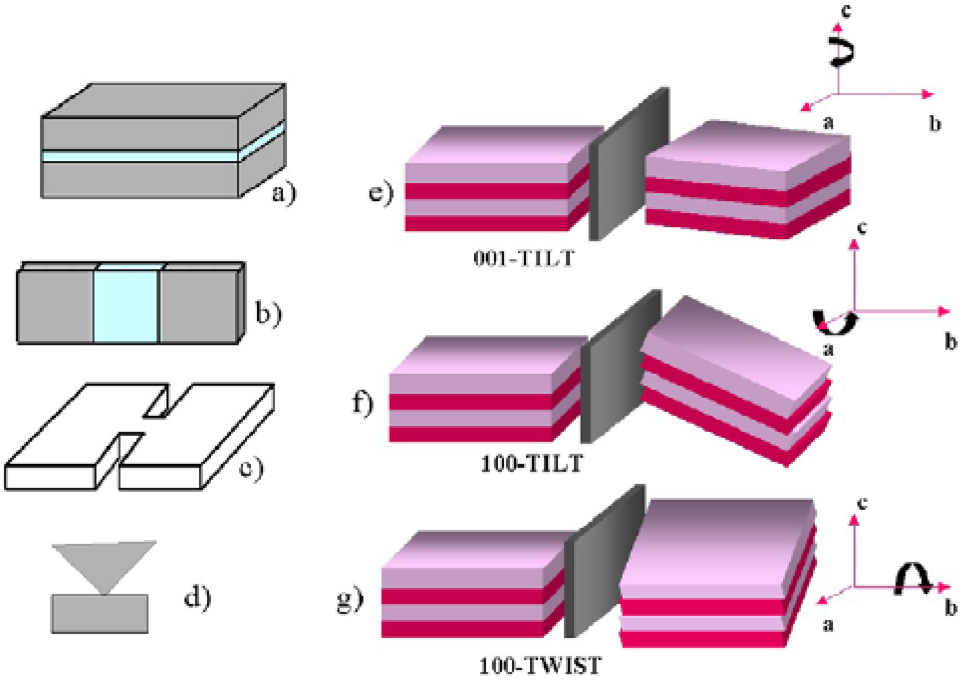

Figure 6.1 Josephson Junction configurations (a) insulating barrier, (b) normal metal barrier, (c) microbridge, (d) point contact, (e)-(g) grain boundary junctions in different orientations. [67]

HTS Josephson junctions are attractive because they can operate at liquid nitrogen temperatures reducing the cost and complexity of the measurement system. However, most HTS Josephson junctions require tedious and multi-step fabrication procedures to form the device [68], [69]. The goal is to provide a simple and reproducible method to produce planar Josephson junctions similar to the microbridge seen in Fig. 6.1(c), using YBCO thin films.

An important class of Josephson junctions is one that employs a planar configuration such as the constriction type weak link or a "Dayem bridge", named after Dayem (1964) who was one of the first to investigate such a structure. The structure can be easily described as two large superconductor regions, typically called banks or reservoirs, linked together by a small narrow bridge or constriction. Such a small constriction or a "weak link" is said to operate as a Josephson junction if the constriction dimensions are on the order of the coherence length (ξ) of the superconductor. Typically these types of structures are fabricated from superconductors which have very large coherence lengths. At zero temperature aluminum has a coherence length of 1600nm, indium is 360nm, and tin is 50nm. For YBCO the coherence length is typically on the order of 1-2nm [4]. Therefore, fabricating a weak link with dimensions comparable to the coherence length of YBCO is not realistic. However, it is still interesting to attempt these weak link structures with YBCO and measure its current-voltage (I-V) characteristics.

The proposed device is similar to the one seen in Fig. 6.1(c). The device was fabricated with the same procedure described in section 3.1. The actual device is shown in Fig. 6.2. The width of the microbridge is 1μm, and the length (distance between 2 superconductor banks) is 2μm.

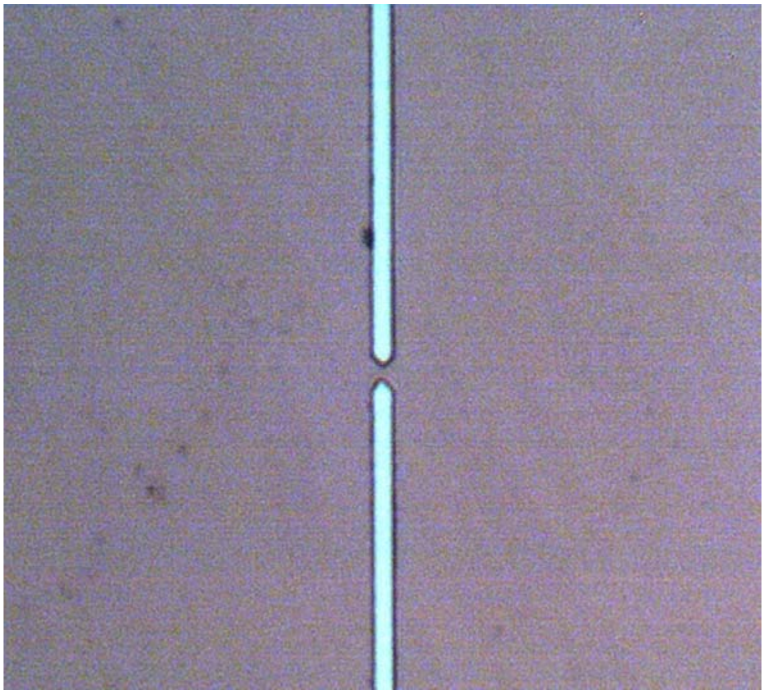

Figure 6.2 YBCO microbridge 1μm width and 2μm length

A typical I-V curve for a Josephson junction is illustrated in Fig. 6.3. There is a clear zero voltage state where current tunnels through the junction. When the current exceeds the critical current of the junction, an abrupt jump is observed with the presence of a finite voltage into a region which appears like a constant resistive slope. For this particular junction when the current is swept backwards, a hysteresis is observed in the I-V curve.

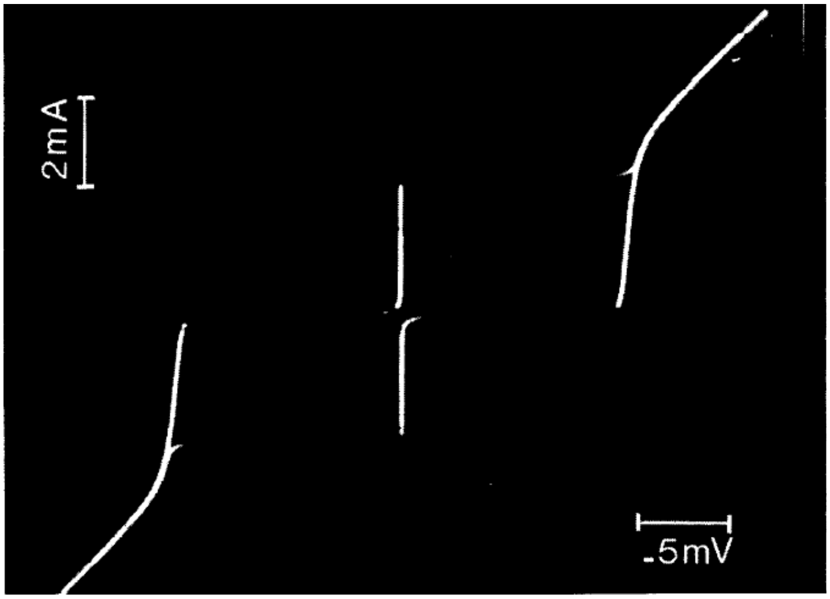

Figure 6.3 Typical I-V curve for a Josephson junction [70]

The I-V curves for the YBCO weak link are measured by four-wire measurement in a Lakeshore DC probe station with four tungsten tip DC probes. A block diagram for the I-V characterization is shown in Fig. 6.4. A current source is used to bias the weak link and a nanovoltmeter measures the voltage across the bridge as shown. Current is applied such that it undergoes a forward and reverse sweep, allowing any hysteresis in the device to be captured. The I-V curve of the weak link is shown in Fig. 6.5. There are two curves red and blue. They are both I-V characteristics of a duplicate device with identical geometry, illustrating that the measurement is repeatable over several devices.

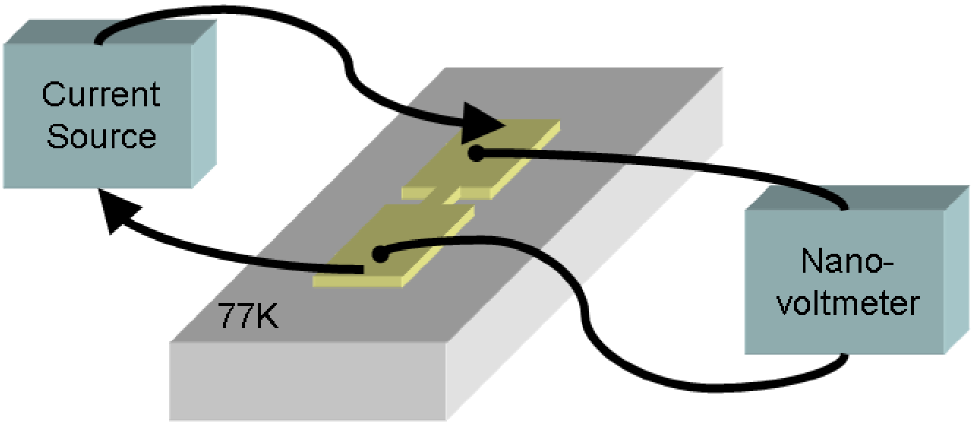

Figure 6.4 Block diagram for YBCO weak link I-V characterization

The I-V curve obtained for the YBCO weak link seems similar to the one in Fig. 6.3. The zero-voltage region is present up to a current of 6.5mA. The finite voltage region is also present, along with the hysteretic behavior of the junction as illustrated by the arrows in Fig. 6.5. The main difference in this junction is the 'voltage creep' region between 6.5mA and 13mA. A magnified view of this region can be seen in Fig. 6.6. The voltage seems to creep off of the zero voltage state to up 13mA until the jump to the resistive region occurs. At this point the reader should note the high values of current and voltage, in the mA and mV range, not typical of classical Josephson junctions.

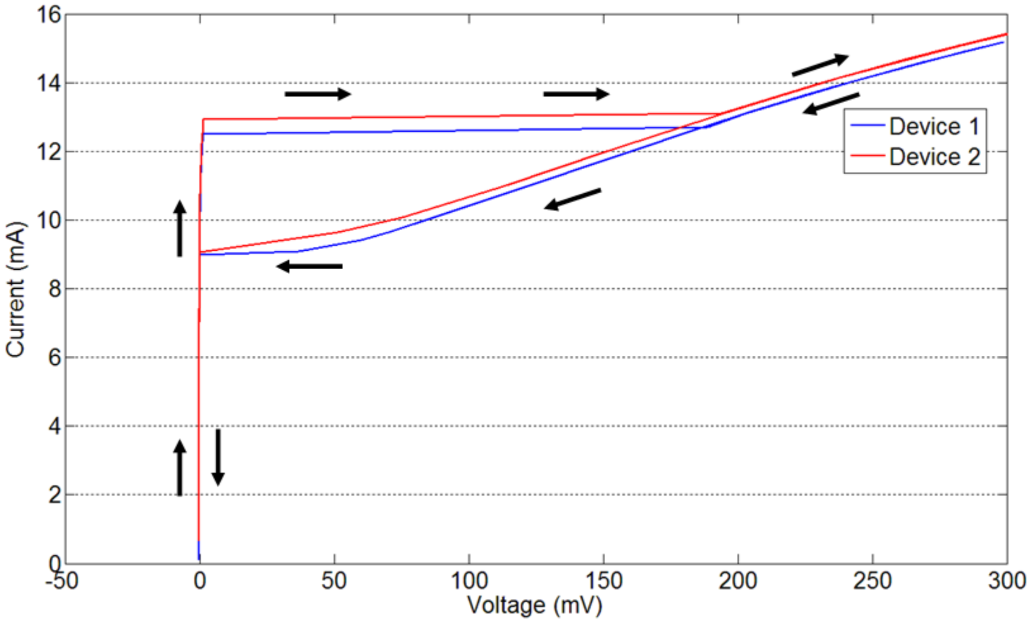

Figure 6.5 Current-Voltage characteristics a YBCO weak link

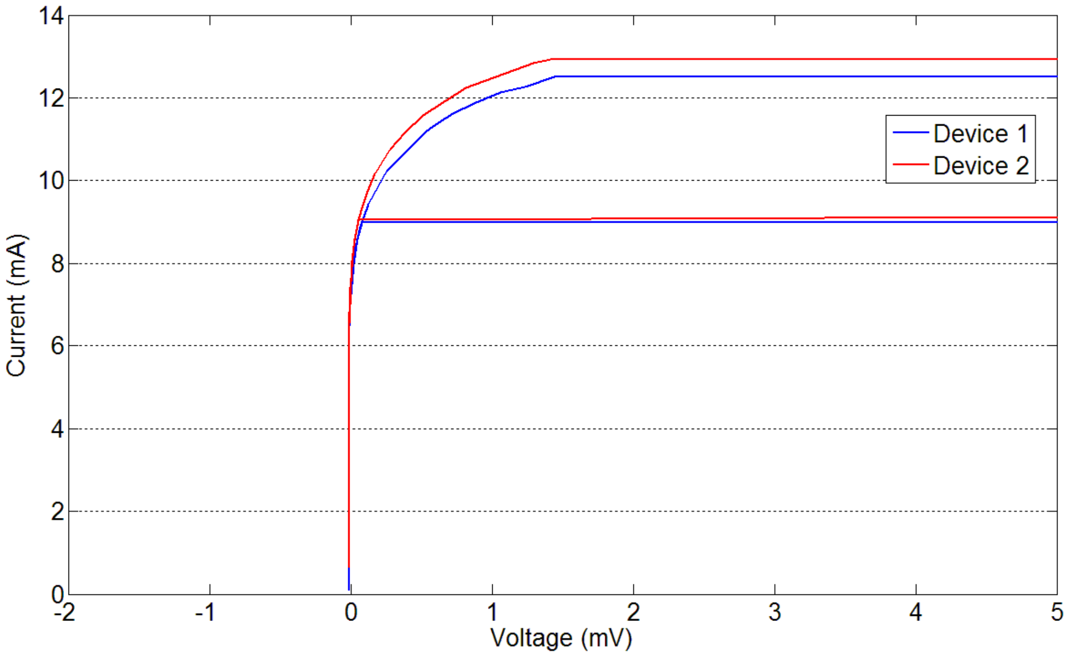

Figure 6.6 Expanded view of the flux flow region in the I-V of a YBCO weak link

The possible interpretation for this result has been suggested by Barone and Huebener [70], [71] but a complete understanding has not yet been achieved. One of the prominent phenomena to consider when examining the voltage carrying state in this structure is the concept of flux flow. In such a structure, when the critical current is reached, the current distribution is no longer uniformly distributed and the zero state voltage becomes unstable. Vortices form and begin to move under the Lorenz force to the center of the bridge, creating what Huebener calls flux tubes. Refer to Fig. 6.7 for an illustration of the vortex motion in the bridge. Although the physics behind the I-V characteristics remains elusive, it is not necessarily important to us. Our interest is to build on this preliminary work, and utilize this I-V characteristic to fabricate the next generation of ultra-sensitive and ultra-high speed detectors.

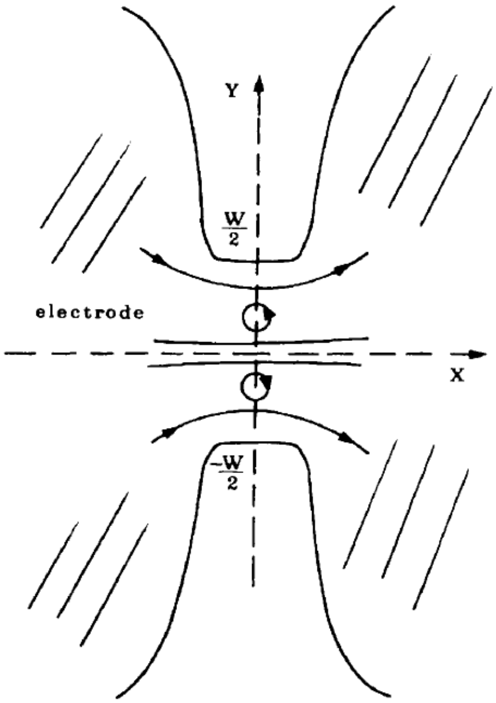

Figure 6.7 Sketch of vortex motion in a weak link [70]

Chapter 7

Conclusions and Future Work

7.1 Results and Conclusions

A microwave photonic cryogenic protestation has been designed and built to characterize HTS optoelectronic devices. Along with microwave probes, the probe station also has a fiber optic probe tip to perform optical excitation experiments on superconducting samples. A methodology to design HTS CPW transmission lines was introduced and experimental data was compared with the theoretical models to show an excellent agreeance.

Several meander line structures were designed to perform an optoelectronic function. These meander line structures were incorporated into the HTS CPW transmission lines. The microwave photonic characterization on the meander lines were performed, characterizing the structures as practical devices, namely a tunable resonator and a tunable delay line. It was shown that a tuning range of up to 2.5GHz could be achieved with the 5µm meander line, and a 90 degree phase shift was achieved with the 3µm meander line.

The photoresponse of the meander line was also investigated under different operating conditions. By varying the current bias and the optical power, both fast and slow photoresponse mechanisms were demonstrated from the 3µm meander line. It was shown that the amplitude of the photoresponse increased linearly below the resistive transition region providing a fast photoresponse, however when the device was driven into a resistive state there was an abrupt increase in the photoresponse amplitude.

YBCO weak links were investigated by measuring the current voltage characteristics of the structure. Although the actual physics behind the I-V curve obtained remains elusive, the goal is to utilize the weak link structure as an ultra-sensitive photodetector at liquid nitrogen temperatures.

7.2 Future Works

By building the foundation to perform optical and microwave measurements in our lab, we propose to design and fabricate new and novel ultra-high sensitivity and ultra-fast photodetectors. The weak link junction shows a lot of potential to achieve this goal. The structure is planar and can easily be adopted into a CPW structure. I have measured the S-parameters of a CPW containing a weak link and it exhibits a negligible effect on the CPW performance. This is a promising result as any photo-generated signal produced in the weak link can efficiently couple and propagate along the transmission line. The challenge lies in efficiently coupling the optical signal to such a small structure.

Appendix A

Fabrication and Characterization of $Tl_2Ba_2CaCu_2O_8$ Thin Films

$Tl_2Ba_2CaCu_2O_8$ or Tl-2212 thin films were deposited on $LaAlO_3$ substrates using a two step process. A precursor thin film layer of BaCaCuO is deposited on the substrates by RF sputtering. This is followed by an ex-situ thallium annealing process of the precursor film in the presence of Tl_2O vapor at 860°C for 60mins. Precursor coated substrates are placed in an alumina crucible along with 0.8g of thallium source powder. The crucible is then tightly sealed with silver foil and placed into a furnace to transform the precursor layer into a Tl-2212 thin film.

Fig. A.1 shows the x-ray diffraction (XRD) pattern of the Tl-2212 film on $LaAlO_{3.}$ It is clear from the figure that we have indeed obtained the correct phase of the Tl-2212 superconductor. The weak peak at 21.2 degrees 2-theta is the Cuk-beta peak associated with the strong $LaAlO_3$ peak. The two peaks at 22.5 and 45.9 degrees 2-theta are the tungsten L peaks associated with the strong $LaAlO_3$ peaks. These tungsten L peaks are normally observed when dealing with strong intensity peaks and are a result of x-ray tube aging.

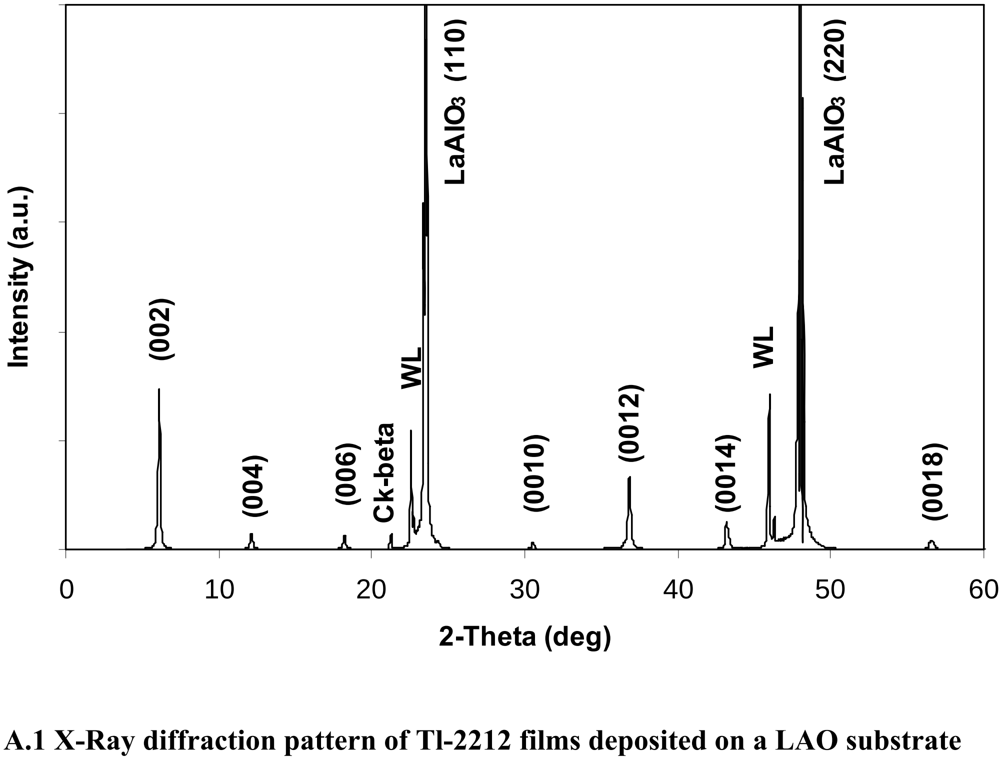

Figure A.1 X-Ray diffraction pattern of Tl-2212 films deposited on a LAO substrate

Optical constants of the Tl-2212 film are obtained for the visible light range at room temperature by ellipsometry. The measurements were obtained using a J.A. Wollam M44 ellipsometer. The film surface was probed at an angle of incidence of 60°, 70°, and 75°, and polarization of 30°. Fig. A.2 shows the index of refraction and extinction coefficient for the TL-2212 thin film. The model used to analyze the ellipsometric data consists of a single Tl-2212 layer film on a LAO substrate. Refractive index values for $LaAlO_3$ were taken from previously measured data and not allowed to vary. The refractive index (n) and extinction coefficient (k) of the Tl-2212 film are described using a combination of three Lorentzian dispersion functions to fit the extinction coefficient, and one Sellmeier function for the real part of the refractive index. The model fit parameters included the film thickness and five dispersion model coefficients. Data was fit using the J.A. Woollam Company WVASE32 software version 3.672.

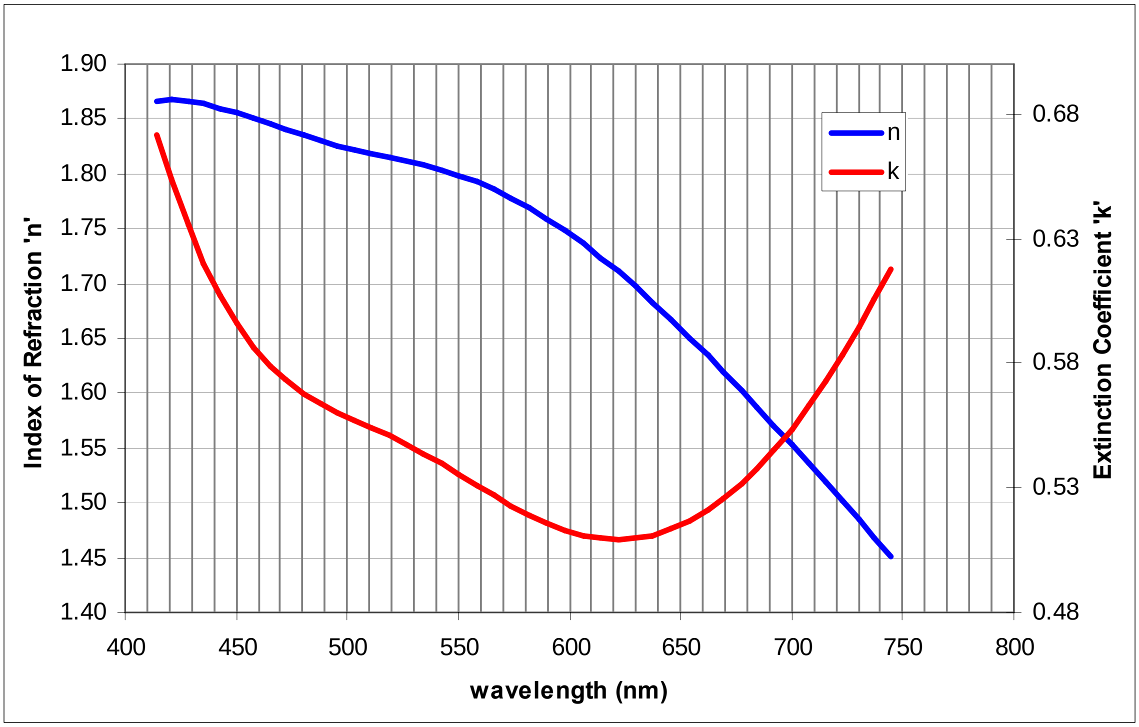

Figure A.2 Optical constants of Tl-2212 obtained by ellispometry

Bibliography

[1] H. Kamerlingh Onnes, *Leiden Commun.* 120b, 122b, 124c, 1911.

[2] W. Meissner and R. Ochsenfeld, “Superconductivty,“ *Naturwissenschaften*, vol. 21, no. 44, pp. 787-788, Nov. 1933.

[3] F. London and H. London, “Electromagnetic Equations of the Supraconductor,” *Proc. R. Soc. Lond.*, A149, pp. 71-88, 1935.

[4] T.P. Orlando and K.A. Delin, *Foundations of Applied Superconductivty*, Addison-Wesley Publishing Company, 1991.

[5] J. Bardeen, L.N. Cooper and J.R. Schrieffer, “Theory of Superconductivity,” *Phys. Rev.*, 108, pp. 1175-1204, 1957.

[6] G. Bednorz and A. Muller, “Perovskite-type oxides—The new approach to high-Tc superconductivity,” *Rev. Mod. Phys.*, vol. 60, no. 3, pp. 585-600, 1988.

[7] R. Sobolewski, “Prospects for high-Tc superconducting optoelectronics,” *Superconductivity and Its Applications, AIP Conference Proceedings 251*, Y.H. Kao, A.E. Kaloyeros, and H.S. Kwok, Eds., pp. 659-670. American Institute of Physics, 1992.

[8] C.H. Lee, “Picosecond optics and microwave technology”, *IEEE Trans. Microwave Theory Tech.*, vol. 38, no. 5, pp. 596-607, 1990.

[9] Y. Enomoto and T. Murakami, “Optical detector using superconducting $BaPb_{0.7}Bi_{0.3}O_3$ thin films,” *IEEE Trans. Microwave Theory Tech.,* vol. 39, no. 12, pp. 2069-2076, 1991.

[10] C.J. Stevens and D.J. Edwards, “Photomixing receiver using the kinetic inductive effect in high Tc superconductors”, *Elec. Lett.*, vol. 37, no. 23, pp. 1420-1421, 2001.

[11] S. Cho and H.R. Fetterman, “Optically tuned propagation delay in YBaCuO superconducting delay lines,” *IEEE Trans. Appl. Superconduct.,* vol. 7, no. 2, pp. 2454-2457, 1997.

[12] Shinho Cho and Chang-Sik Son, “Modulation of the Resonance Frequency of Superconducting Microwave Resonators,” *IEEE Trans. Appl. Superconduct.,* vol. 13, no. 2, pp. 3659-3662, 2003.

[13] G. J. Hofer, F. Jager, and H. A. Kratz, “Broadband four-channel cryogenic wafer probing system for automated coplanar on-chip measurements,” *Rev. Sci. Instrum.,* vol. 64, no. 3, pp. 788-792, 1993.

[14] J. Lasker and J. Kolodzey, “Cryogenic vacuum high frequency probe station,” *RJ. Vac. Sci. Technol. B.,* vol. 8, no. 5, pp. 1161-1165, 1990.

[15] S. R. Taub, S. A. Alterovitz, P. G. Young, B.T. Ebihara and R. R. Romanofsky, “Cyrogenic Probe Station for use in Automated Microwave and Noise Figure Measurements,” *NASA technical memorandum 106560,* 1994.

[16] J. J. Bautista, J. Laskar and P. Szydlik, “On-Wafer, Cryogenic Characterization of Ultra-Low Noise HEMT Devices,” *TDA Progress Report 42-120,* 1995.

[17] Jack W. Ekin, *Experimental Techniques for Low-Temperatures Measurements*, Oxford University Press, 2006, section 3.3.

[18] No author listed, “Application Note: On-Wafer Vecotr Network Analyzer Calibration and Measurements,” Cascade Microtech.

[19] No author listed, “Corning® SMF28 optical fiber Product Information,” Corning Inc., Corning, NY, Apr. 2002.

[20] M.K. Wu, *et al.*, “Superconductivity at 93 K in a new mixed-phase Y-Ba-Cu-O compound system at ambient pressure,” *Phys. Rev. Lett.,* vol. 58, no. 9, pp. 908-910, 1987.

[21] F. A. Hegmann, “Picosecond Photoresponse of High-Tc Superconducting Thin Films,” Ph.D. dissertation, Dept. Phys., McMaster Univ. Hamilton, ON, 1994.

[22] N.W. Ashcroft, and N.D. Mermin, *Solid State Physics,* Harcourt Brace College Publishers, 1976.

[23] Alan M Portis, *Electrodynamics of High-Temperature Superconductors,* World Scientific Publishing, 1992.

[24] J. L. Vossen and W. Kern, *Thin Film Processes II*, Academic Press, Boston, MA, 1991, section II-4.

[25] D.Dijkkamp, T. Venkatesan, *et al.*, “Preparation of Y-Ba-Cu oxide superconductor thin films using pulsed laser evaporation from high Tc bulk material,” *Appl. Phys. Lett.,* vol. 51, no. 8, pp. 619-621, 1987.

[26] M. A. Herman and H. Sitter, “Molecular Beam Epitaxy: Fundamentals and Current Status", Springer, New York, 1996.

[27] S. Sivaram, “Chemical Vapor Deposition: Thermal and Plasma Deposition of Electronic Materials", Van Nostrand Reinhold, New York, 1995.

[28] Theva Film Deposition by thermal co-evaporation. [Online] Available: http://www.theva.com/index.php?option=com_content&task=view&id=50&Itemid=55

[29] B. Utz *et al*, “Deposition of YBCO and NBCO Films on Areas of 9 Inches in Diameter,” *IEEE Trans. App. Supercond.*, vol. 7, no. 2, pp. 1272-1277, 1997.

[30] Hitachi High-Technologies Europe. [Online] Available: http://www.hht-eu.com/cms/15805.html

[31] Y. Nishi, *et al*, “Oxygen ion etching of YBa2Cu3O7−y,” *Nucl. Instruments Methods in Physcics Research*, vol. 59-60, part 2, pp. 1415-1417, 1991.

[32] R. Liang, D.A. Bonn, W.N. Hardy, “Growth of high quality YBCO single crystals using BaZrO3 crucibles,” *Physica C*, vol. 304, issue 1-2, pp. 105-111, 1998.

[33] M. J. Lancaster, *Passive Microwave Device Applications of High-Temperature Superconductors*, Cambridge University Press, 1997.

[34] H. R. Mohebbi and A. Hamed Majedi, “CAD model for circuit parameters of superconducting-based hybrid planar transmission lines,” *Supercond. Sci. Technol.*, vol. 22, 2009.

[35] A. H. Majedi, S. K. Chauduri, and S. Safavi-Naeini, “Optical-microwave interaction modeling in high-temperature superconducting films,” *IEEE Trans. Microw. Theory Tech.*, vol. 29, no.10, pp. 1873-1881 2001.

[36] Z. Yan, and A. H. Majedi, “Physical modeling of hot-electron superconducting single-photon detectors,” *IEEE Trans. Appl. Superconduct.*, vol. 17, no.3, pp. 3789-3794, 2007.

[37] D.M. Pozar, *Microwave Engineering*, Addison-Wesley Publishing Company, 1990.

[38] R.E. Collin, *Foundations for Microwave Engineering*, McGraw-Hill, 1992.

[39] R.N. Simons, *Coplanar Waveguide Circuits, Components, and Systems*, Wiley, 2001.

[40] B. C. Wadell, *Transmission Line Design Handbook.*, Artech House, 1991.

[41] G. Hasnain, A. Dienes, and J. R. Whinnery, "Dispersion of Picosecond Pulses in Coplanar Transmission Lines," *IEEE Trans. Microw. Theory Tech.*,, vol. 34, no. 6, pp. 738-741, Jun. 1986.

[42] W. Rauch and E. Gornik, *et al.*, "Microwave properties of YBa2Cu3O7−x thin films studied with coplanar transmission line resonators," *Appl. Phys. Lett.*, vol. 73, pp. 1866-1872, Feb. 1993.

[43] A. Valenzuela, G. Solkner, *et al.*, "Microwave characterization of structured YBa2Cu3O7−x-thin films," *Mater. Sci. Forum,* vol.30–132 349–372.

[44] O. G. Vendik, I. B. Vendik, D. I. Kaparkov, "Emperical model of the microwave properties of high-temperature superconductors," *IEEE Trans. Microw. Theory Tech.,* vol.46, no. 5, pp. 469-478.

[45] F.A. Hegmann and J.S. Preston, "Origin of the fast photoresponse of epitaxial YBa2Cu3O7−x thin films," *Appl. Phys. Lett.*, vol. 48. no. 21, pp. 16023-16039, Dec. 1993.

[46] C. Caloz, and T. Itoh, *"Electromagnetic Metamaterials: Transmission Line Theory and Microwave Applications,"* Wiley-Interscience, 2006.

[47] S. Cho and C. Lee, "Electrical and thermal modulation of the propagation time in superconducting spiral lines by optoelectronic techniques," *IEEE Trans. Applied Supercond.,* vol. 11, pp. 127–130, March 2001.

[48] S. Cho and S. Son, "Modulation of the Resonance Frequency of Superconducting Microwave Resonators," *IEEE Trans. Applied Supercond.*, vol. 13, no. 2., pp. 3659-3662, June 2003.

[49] D. Lederman, *et al.*, "Photoinduced superconductivity and structural changes in high temperature superconducting films," *Appl. Phys. Lett.*, vol. 64, pp. 652–654, Jan. 1994.

[50] G. Nieva, *et al.*, "Photoinduced enhancement of superconductivity," *Appl. Phys. Lett.,* vol. 60, pp. 2159–2161, April 1992.

[51] R. S. Nebosis, *et al.*, "Ultrafast photoresponse of an YBaCuO film to far-infrared radiation pulses," *Opt. Lett.,* vol. 18, pp. 96–97, Jan. 1993.

[52] S. Cho, *et al.*, "Electrical tuning of the kinetic inductance of high temperature superconductors," *Appl. Phys. Lett.,* vol. 65, pp. 3389–3391, Dec. 1994.

[53] E.K. Track, R.E. Drake, and G.K. G. Hohenwarter, "Optically modulated superconducting delay lines," *IEEE Trans. Applied Supercond.*, vol. 3, no. 1., pp. 2899-2902, June 1993.

[54] D. Zhang., *et al.*, “Optical control of millimeter wave high Tc superconducting quasi-optical bandpass filters,” *Appl. Phys. Lett.,* vol. 58, pp. 1560-1562, Apr. 1991.

[55] M. Tsindlekht, *et al.*, “Frequency modulation of the superconducting parallel-plate microwave resonator by laser irradiation,” *Appl. Phys. Lett.,* vol. 65, pp. 2875-2877, Nov. 1991.

[56] S. M. Anlage, H.J. Snortland, and M. R. Beasley, “A current controlled variable delay superconducting transmission line,” *IEEE Trans. Magn.*, vol. 25, pp. 1388-1391, Mar. 1989.

[57] G.L. Carr, *et al.*, “Fast bolometric response by high-Tc detectors measured with subnanosecond synchrotron radiation,” *Appl. Phys. Lett.,* vol. 57, pp. 2725-2727, Dec. 1990.

[58] A. Rothwarf and B. N. Taylor, “Measurement of Recombination Liftimes in Superconductors,” *Phys. Rev. Lett.*, vol. 19, no.1, pp. 27-30, July 1967.

[59] C. S. Owen and D. J. Scalapino, “Superconducting states under the influence of external dynamic pair breaking,” *Phys. Rev. Lett*., vol. 28,no.24, pp. 1559-1561, June 1972.

[60] G. A. Sai-Halasz, *et al.*, “Effect of dynamic external pair breaking in superconducting films,” *Phys. Rev. Lett.*, vol. 33, no. 4, pp. 215-219, July 1974.

[61] N. Perrin and C. Vanneste, “Response of superconducting films to periodic optical irradiation,” *Phys. Rev. B*, vol. 28, no. 9, pp. 5150-5159, Nov. 1983.

[62] A. Frenkel, “Mechanism of nonequilibrium optical response of high temperature superconductors,” *Phys. Rev. B,* vol. 48, no. 13, pp. 9717-9725, Oct. 1993.

[63] M. Lindgren, *et al*, “Ultrafast photoresponse in microbridges and pulse propagation in transmission lines made from high-Tc superconducting thin films,” *IEEE J. Sel. Topics Quantum Electron.*, vol. 2, no. 3, pp. 668678, Sep. 1996.

[64] R. Adam, *et al*, “Picosecond response of optically driven Y-Ba-Cu-0 microbridge and Josephson junction integrated structures,” *IEEE Trans. Appl. Supercond.*, vol. 9, no. 2, pp. 4091-4094, June 1999.

[65] A. H. Majedi, *et al*, “Analysis of kinetic inductance photoresponse of high-Tc superconducting films,” in *Integrated Photonics Research (IPR) Conference Technical Digest,* pp. 88-90, Quebec, Canada, July 2000.

[66] F.A. Hegmann, and J.S. Preston, “Origin of the fast photoresponse of Epitxial YBa2Cu3O7−x thin films,” *Phys. Rev. B,* vol. 48, no. 21, pp. 16023-16039, Dec. 1993.

[67] F. Tafuri and John R. Kirtley,, “Weak links in high critical temperature superconductors,” *Rep. Prog. Phys.,* vol. 68, pp. 2573-2663, July 2005.

[68] W. F. Staden, *et al.*, “A novel buffered high-Tc superconducting step-edge Josephson junction,” *Supercond. Sci. Technol.,* vol. 20, pp. S419-S425, July 2007.

[69] M. H. Bae, *et al.*, “Zero-crossing Shapiro steps in high Tc superconducting microstructures tailored by focus-ion beam,” *Phys. Rev. B,* vol. 77, id. 144501, Apr. 2008.

[70] A. Barone, G. Paterno, *Physics and Applications of the Josephson Effect*, John Wesley & Sons, 1982.

[71] R. P. Huebener, *Magnetic Flux Structures in Superconductors*, Springer-Verlag Berlin Heidelberg New York, 1979.